

Microtechnology Department

Head: Gábor BATTISTIG, Ph.D.

Research Staff

- István BÁRSONY, Member of HAS.,
- László DÓZSA, Ph.D.,
- Péter FÜRJES, Ph.D.,
- Zoltán LÁBADI, Ph.D.,
- György MOLNÁR, Ph.D.,
- Anita PONGRÁCZ, Ph.D.,
- Vilmos RAKOVICS, Ph.D.,
- Zsolt ZOLNAI, Ph.D.
- Ágoston NÉMETH, Ph.D.,
- Andrea Edit PAP, Ph.D.,
- Antalné ÁDÁM, M.Sc., (part time)
- Albert KARACS, M.Sc., (part time)
- Tibor MOHÁCSY, M.Sc., (part time)
- Ákos NEMCSICS, Ph.D. (part time)
- Gábor PETŐ, D.Sc., Prof. Emeritus
- Bálint PÓDÖR, Ph.D. (part time)
- Zsolt József HORVÁTH, D.Sc., (part time)
- Béla SZENTPÁLI, Ph.D., (part time)
- Éva VÁZSONYI, M.Sc., (part time)

Ph.D. students / Diploma workers

- Zsófia BAJI, Ph.D. student
- Ferenc BIRÓ, Ph.D. student
- Réka CSUTAK, Ph.D. student
- Zoltán FEKETE, Ph.D. student
- Tamás KÁRPÁTI, Ph.D. student
- Gergely MÁRTON, , Ph.D. student
- Balázs BENEDEK, M.Sc. diploma w.
- Péter BERINKEI, M.Sc. diploma w.
- Péter NAGY, M.Sc. diploma w.
- Ferenc TOLNER, M.Sc. diploma w.

Technical Staff

- György ALTMANN, technician
- Edvard BADALJÁN, engineer
- Gabriella BIRÓ, technician
- Sándor CSARNAI, technician
- Tibor CSARNAI, technician
- Ábel DEBRECZENY, engineer (part time)
- Magdolna ERŐS, technician
- Csilla ARIAS-SOTONÉ FARAGÓ, technician
- János FERENCZ, engineer
- Róbert HODOVÁN, engineer
- Csaba LÁZÁR, engineer
- András LŐRINCZ, engineer
- Ákos MAJOROS, engineer
- Attila NAGY, technician
- Károlyné PÁYER, technician
- István RÉTI, engineer
- Ádám SZENDREY, engineer
- Magda VARGA, technician
- Katalin Veresné-VÖRÖS, engineer
- Sándor PÜSPÖKI, engineer (part time)
- Zsuzsa PÜSPÖKI, engineer (part time)
- Imre SZABÓ, engineer, dr. Univ. (part time)
- Tamás SZABÓ, engineer (part time)

The mission of the Microtechnology Department is the research, development and system integration of physical, chemical/biochemical sensors and systems:

- MEMS and MEMS related technologies, with special emphasis on development 3D microstructures;
- Development and functional testing of different MEMS based gas, chemical, 3D force, thermal, biology related sensors and sensor systems;
- Development of micro- and nanofluidic components and systems;
- Development and applications of near IR light emitting diodes and detectors;
- Development of solar cells and their competitive technology.

Fundamental research on:

- sensing principles;
- novel materials and nanostructures;
- novel 3D fabrication techniques;
- ion-solid interaction for supporting MEMS development.

Device and material characterizations widely used in our projects:

- Ion beam analysis methods;
- IR and Raman scattering;
- Scanning Microprobes;
- Optical and Electron Microscopy, SEM, TEM, EDX;
- Spectroscopic Ellipsometry;
- Electrical characterisations
- Microfluidic and biofunctional characterisation.

The Microtechnology Department of MFA runs the 300 sqm clean lab (Class 100-10000) with the complete Si-CMOS technology together with a mask shop, unique in Hungary. The CIGS solar cell technology laboratory equipped with a pilot line of sputtering, evaporation and laser scribing modules for 30×30 cm² glass substrates is also connected to the clean lab facility.

The technology base of the clean lab has been further improved in the recent years. In 2011 a new Heidelberg DLW66 type laser pattern generator was purchased and installed in our mask shop. The new facility allows us to produce 4"-8" masks with 1 micrometer linewidth. Direct writing of the pattern to the surface of a photoresist coated wafer is also possible by the DWL66 laser writer.

Main technologies available in the Microtechnology lab for our partners and customers:

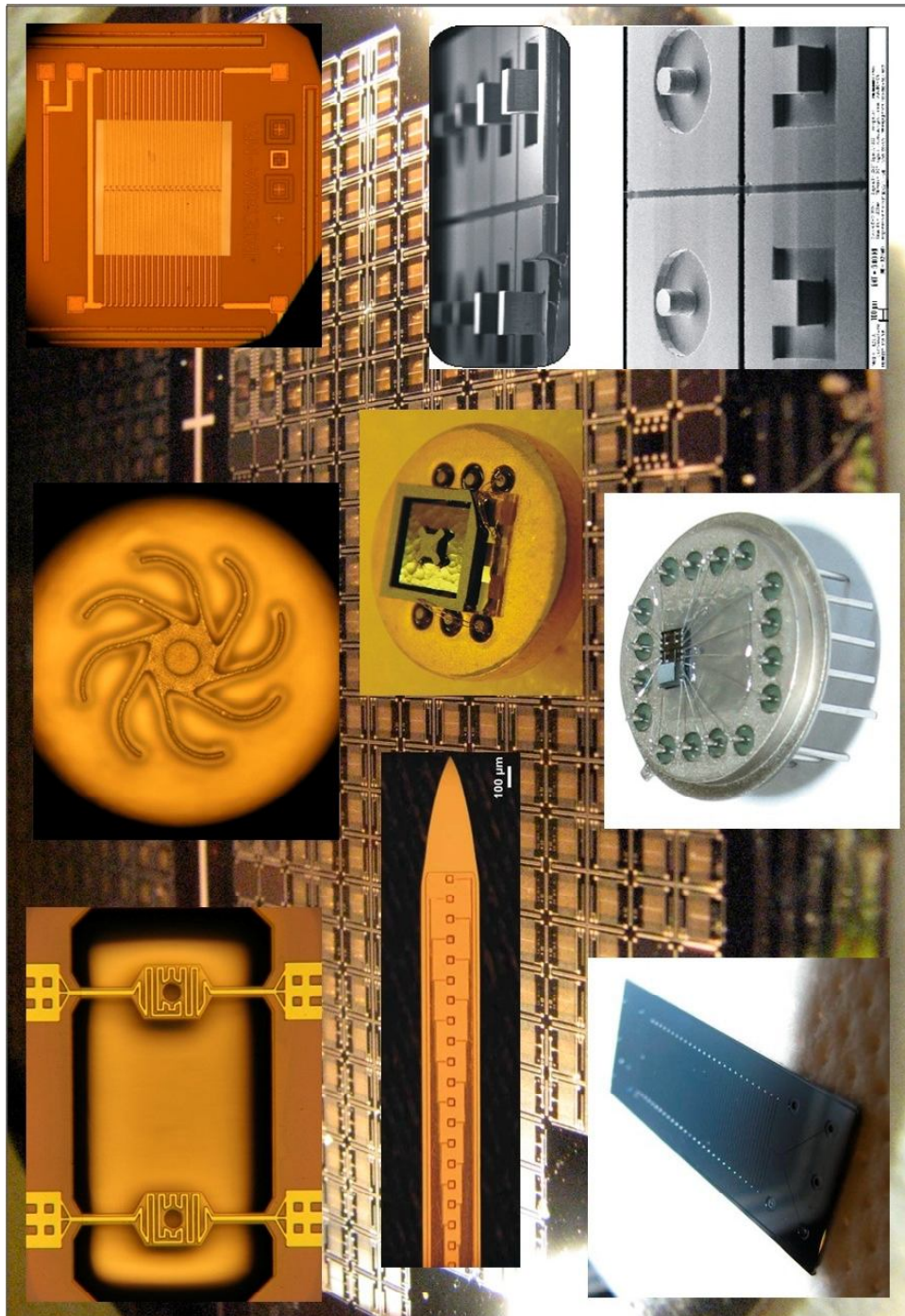
- High temperature annealing, diffusion and oxidation
- Rapid Thermal Treatment
- Low Pressure Chemical Vapor Deposition of poly-Si, SiO₂ and Si₃N₄ layers
- Low Temperature Chemical Vapor Deposition
- Ion implantation
- Thin film depositions – Electron beam evaporation, DC and RF Sputtering

- Atomic Layer Deposition
- Deep Reactive Ion Etching
- Photolithography with back-side alignment and Nanoimprinting
- Wafer Bonding
- Wet chemical treatments
- Electro-chemical porous Silicon formation
- Molecular Beam Epitaxy of III-V compound semiconductors
- Mask design, laser pattern generator and laser writer
- Polymer structuring by photolithography and micromoulding techniques
- Electrical and functional characterizations

Overview of the MFA Microtechnology clean lab



MEMS devices developed in the MFA MEMS lab.



**Micro- and nanofluidic elements and devices developed in
MFA Microfluidics lab.**



Tyre integrated shear force sensor

(ENIAC JU SE2A)

I. Bársony, A. Pongrácz, M. Ádám, Z. Hajnal, A. Nagy, and G. Battistig

In the frame of the SE2A ENIAC project the MFA MEMS Lab in close cooperation with WESZTA-T Ltd developed a tyre integrated shear force sensor using the Si 3D force sensor in a special package integrated on the sidewall of the tyre.

The Si force sensor is integrated into a rubber patch and this patch is placed on the sidewall of the tyre. Tyre repair patch is a widely used and reliable solution, does not interfere with the tyre deformation, therefore it is suitable for the encapsulation of the sensing element.

A real tyre was analyzed and a complex FEM simulation model was created in order to define the appropriate placement of the patch-encapsulated sensor. The geometric model used in simulations is a simplified version of the real composite structure used in radial tyres. Nonlinear Mooney-Rivlin 2 constant material model was used in early simulations, which was later replaced by a linearized model. Comparing the results of the measurements and the simulations the maximum amount of difference in deformation is less than 15%. In the next stage the FEM simulation model was used to determine the best position of the sensor system.

A measurement construction was built by WESZTA-T Ltd, which is able to cause different stresses in 3 directions in a fixed car-wheel. The measurement board, which contacts with the wheel, can be moved in 3 direction (vertical, lateral and longitudinal force) the forces can be increased up to 2200 kg. Exact value of the forces can be measured using load cells in each direction with 0.1% accuracy. The surface of the measurement board is asphalt, to provide real circumstances.

A $2 \times 2 \text{ mm}^2$ sensor was integrated in the tyre using the rubber patch assembly and was tested under different loads using the measurement setup described above. Inductive supply and communication was tested on a rotating tyre. Reliable communication is working up to 8cm distance with 5mW transmitted power at 60km/h speed.

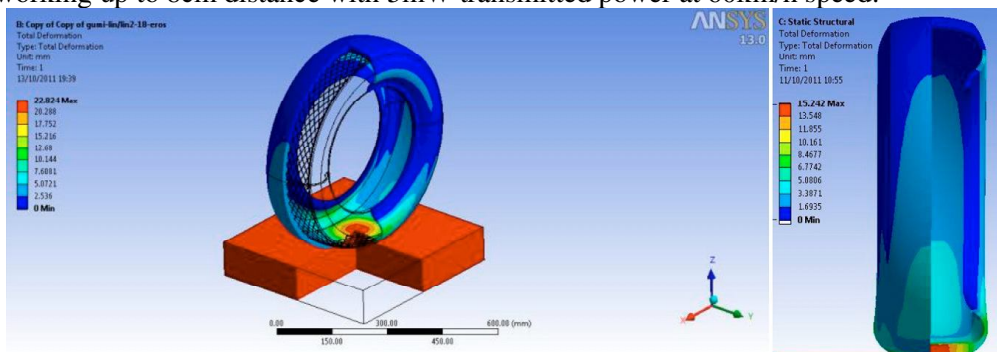


Figure 1. Tyre deformation simulated in ANSYS using 0.22 MPa internal pressure and 2 kN load.

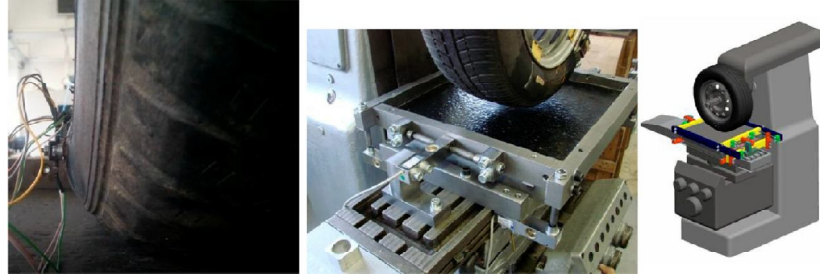


Figure 2. Sensor is mounted on the sidewall of a tyre using a rubber patch (left). The applied load is 2 kN. Measurement pad with 8 load cells is shown on the right with a schematic illustration.

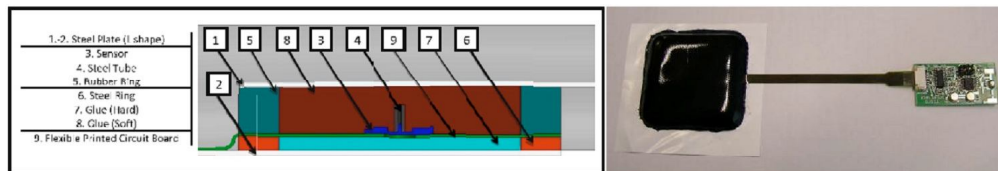


Figure 3. Schematic of the sensor packaging (left) and the realized unit (right).

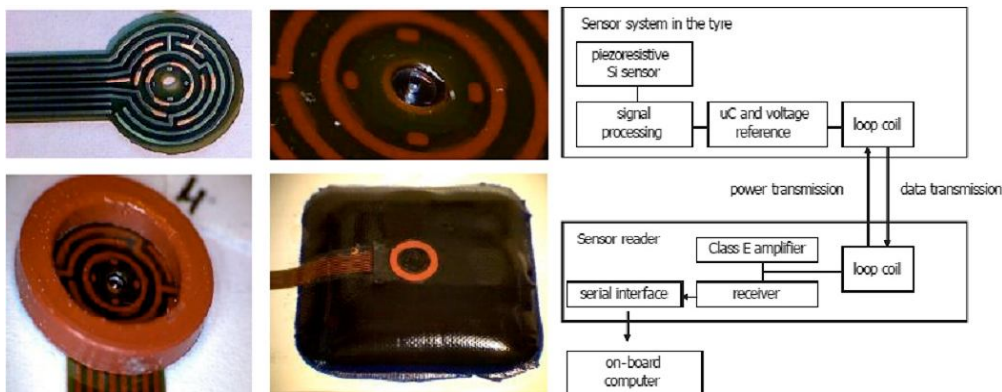


Figure 4. Sensor packaging step-by-step. a) flexible PCB b) Si chip mounted in the center of the PCB c) rubber spacers d) sensor in the rubber patch e) sensor in the rubber patch assembly ready for installation. Diagram of the system built-in the tyre (right).

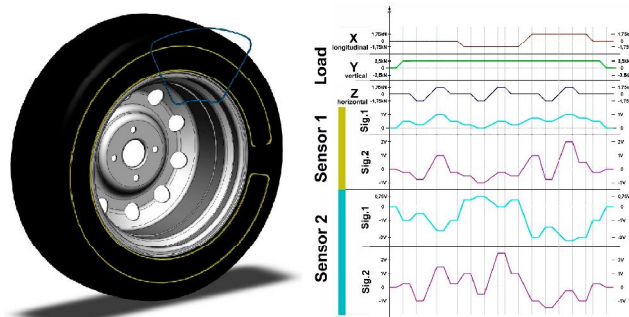


Figure 5. Sensor signals versus different x-y-z loads (left). Shape and positioning of the standing (blue) and rotating (yellow) loop coil on tyre for the wireless communication and suppl.

Glue free packaging development of the full membrane 3D force sensor using wafer bonding

(ENIAC JU SE2A)

I. Bársony, A. Pongrácz, M. Ádám, Z. Hajnal, A. Nagy, and G. Battistig

Micromachined 3D force sensors gain importance not only in the field of tactile sensing, robotics and biomedical sciences, but also in automotive applications. Development of a sensor-specific packaging technology for the piezoresistive force sensors is a crucial object in order to eliminate or minimize the functional instabilities generated by the system level thermal and thermomechanical effects.

The developed design and process flow [É. Vázsonyi, M. Ádám, Cs. Dücső, Z. Vízváry, A. L. Tóth and I. Bársony: Sensors and Actuators, A 123-124 (2005), pp.620-626.] was improved by an additional hybrid wafer bonding step consisting of a simultaneous anodic and metal fusion bonding process. Using the glass substrate improves thermal isolation and thermo-mechanical stability of the system. Because of the thermal expansion coefficients of the chosen glass and the Si-only slightly differ, the residual thermomechanical stress during the operation is minimized.

The technology involves the formation of piezoresistors on the backside of a thin Si membrane, while on the front side a circular silicon rod is emerging out of the center of the membrane produced by subtractive dry etching (Deep Reactive Ion Etching) technology. A hybrid wafer bonding (Si to glass and Al to Al) facilitates the reliable signal read-out from the ion-implanted piezoresistors and ensures the thermal isolation of the sensing elements and the packaging. Through-wafer Si etching opens up windows over the contact pads of the glass carrier wafer making the pads accessible for wire bonding.

In Figure 3 the optical image of a successfully bonded structure is shown. Our recently presented procedure enables parallel cavity formation, metal outlet fabrication from backside, electrical and mechanical bonding of the sensor chip to a glass carrier wafer, while keeping the chip thermally isolated and minimizing the sensitivity of the functional parameters to the thermomechanical effects which has crucial importance in the planned biomedical and automotive applications.

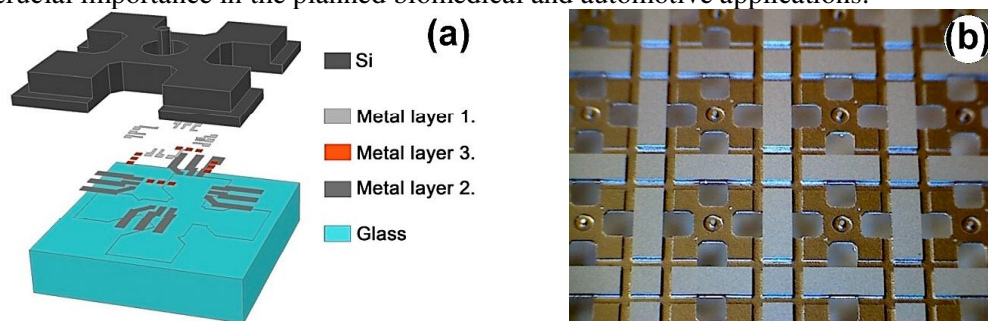


Figure 1. (a) Schematic cross section of the structure, (b) Wafer level realization of the Si 3D force sensor

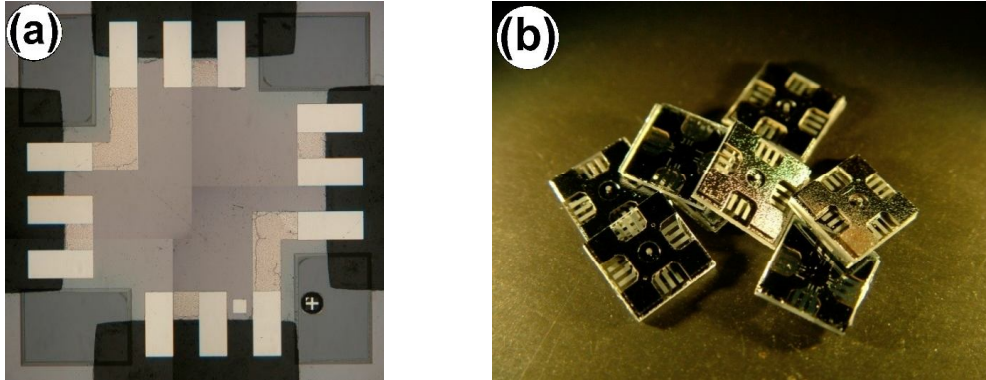


Figure 2. (a) An optical image of the hybrid bonded test structure from glass side. (b) A bunch of 3D force sensors with the realized Si/glass heterostructure.

THz detectors

B. Szentpáli, G. Battistig, P. Fürjes, A. Pongrácz, P. Földesy

The development of the THz detector was continued under the OTKA project TERASTART. The principal structure of the device and the photo of a chip are shown in Fig. 1.

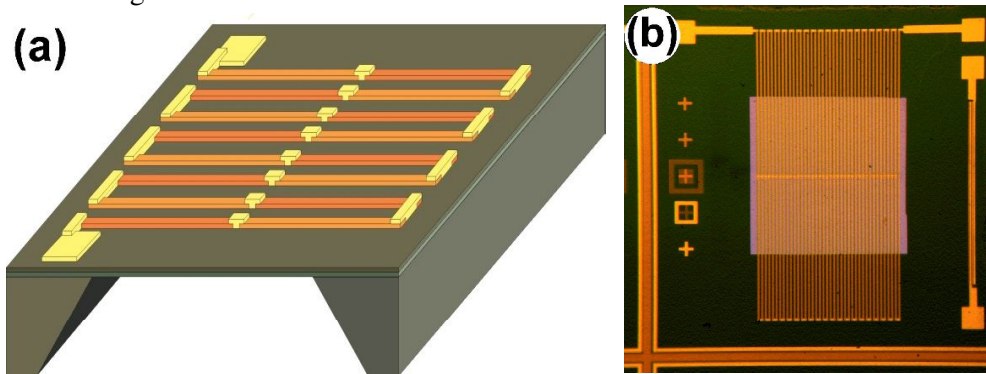


Figure 1. (a) the schematic of the device. (b) the photo of the chip. The chip size is $2 \times 2 \text{ mm}^2$, it holds 40 linearly arranged thermocouples.

The thermocouple lines act as short circuited dipole antennas, in which the distribution of the induced current is sinusoidal, having the maximum value at the center. Therefore the associated Joule heat formation reaches its maximum also around the middle of the lines, exactly where it generates the highest thermoelectric effect. The thermocouple lines are composed from p- and n-type poly-silicon, deposited by LPCVD process at 630°C with SiH_4 as the precursor. The p- and n-type parts are ion-implanted by B and P respectively. The doping concentrations were determined in such a way that they result in the same electrical conductivity as far as

possible in order to ensuring the electric symmetry of the antennas. The membrane is a double layer of non-stoichiometric silicon-nitride (SiN_x) and silicon-oxide (SiO_2) with the appropriate thickness ratio resulting enhanced mechanical stability and minimizing the residual stress in the suspended membrane area. The antenna-like operation was demonstrated by the strong dependence on the polarization of the high-frequency radiation, as it is shown in Fig. 2.

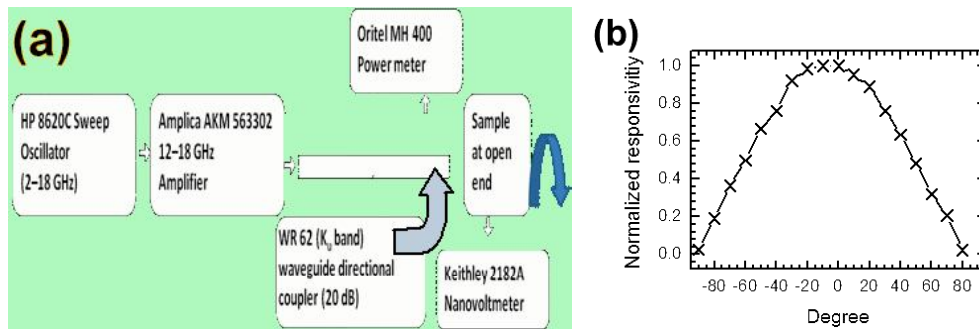


Figure 2. (a) The set-up for measuring the responsivity at 13 GHz, (b) The output in the function of the polarization angle. The maximum is obtained when the electric field is parallel to the thermocouple lines.

In the THz band two measurements were performed: at 100 GHz and in a broad-band THz radiation. The 100 GHz signal was generated by successive multiplication of the microwave power and radiated to the chip by a W-band horn antenna. The broad-band THz signal was produced by the excitation of a non-linear crystal (LiNbO_3) by ps laser pulses. Beyond these investigations the responsivity to infrared radiation was also measured. The source was a heated black body formed from a $5 \times 5 \text{ cm}^2$ aluminum plate covered by “black velvet” paint. Its temperature was regulated by a controlled Peltier element between 0...100 °C. The results are summarized in the Table I.

Table I. The responsivities of the same chip to different excitations.

excitation	13 GHz	100 GHz	Broad-band THz	Black-body radiation
responsivity [V/W]	0.2	5.6	21	20
coupling factor	0.22%	6.2%	23.3 %	22.2 %

The coupling factors are the ratios of the estimated responsivities and the 90 V/W, the responsivity to the direct electric heating, which can be considered as an absolute reference value. This value was obtained on a kindred structure having an integrated electric heater on the chip. The recorded data clearly indicate that the efficiency increases with the increase of the frequency, further the responsivities to IR and to the broad-band THz are very close. The coupling factor of the THz radiation is rather high, competitive with other published values of THz detectors with different working principles.

MEMS Capacitive pressure sensor

T. Kárpáti, A. E. Pap, A. Adam, and A. Pongrácz

Pressure sensing systems are used in many applications such as automation in manufacturing industries, medical applications, monitoring in vehicle industry and so on. The pressure sensors and transducers transform the induced force in a sensing area to displacement or mechanical stress. In many case the industrial applications showed that measuring is required at low pressure range. Our silicon based capacitance pressure sensor with the range under 1000 mbar was developed in co-operation of the MFA and Weszta-T Ltd.

The sensor is built up from two parts; single crystalline Si membrane electrode and the carrier Borofloat 33[®] glass with aluminum capacitor plate (fix electrode) and bonding pads (See Fig. 1.).

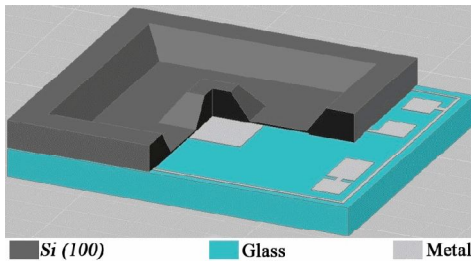


Figure 1. Diagram of silicon-based capacitance pressure sensors.

The thin diaphragm was formed by using an anisotropic alkaline etching combined with Electro-Chemical Etch Stop. The initial thickness of Si wafer was set at the center and round the side of the chip. The total thickness frame on the chip side serves the electrode mechanical strength, the good tractability during technology methods. Due to the center reinforcement the capacitor structure behaves like a parallel capacitor once the membrane

deforms. In order to promote free moving of the membrane during the bonding method and for the outlet of the fix electrode a cavity on the bottom side of the Si chip was etched. The static bottom electrode on glass substrate was realized by aluminum evaporation and it was patterned by etching technique. The fabricated structures are presented in Figs. 2-3.

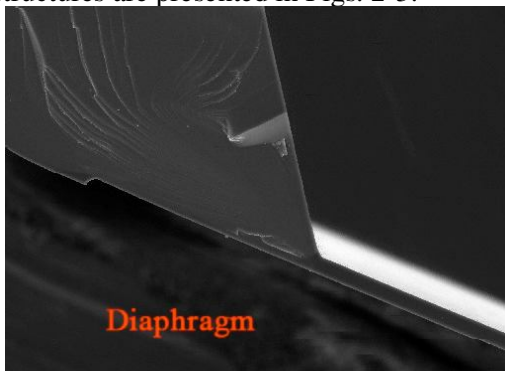


Figure 2. The free standing silicon membrane forming the moving electrode of the capacitor fabricated by bulk micromachining.

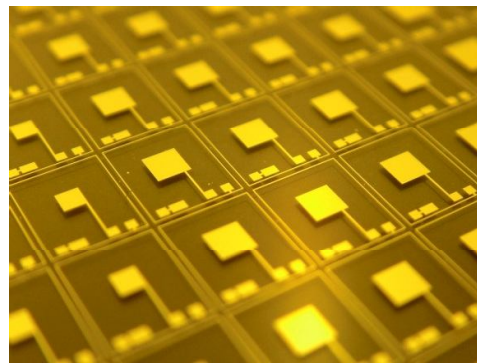


Figure 3. Metal electrodes of the capacitive sensors realized on glass wafer.

Finally, the 500 μm thick metalized Borofloat 33[®] glass with the Al pattern and the structured silicon wafers were anodically bonded at low temperature ($T=200\text{ }^{\circ}\text{C}$) which guaranteed a very high mechanical strength. For anodic bonding the wafers was aligned by a SÜSS MicroTech MA6/BA6 type Mask Aligners. The equipment is adapted for two side mask alignment, which facilitates to form the diaphragm structure. After the alignment, the clamped wafer pair was bonded by the SÜSS MicroTech SB6L wafer bonder device. The applied parameters of anodic bonding were 200°C temperature, -1000 V voltage, 1000 mbar tool pressure, 40 min process time, and the procedure made under 10^{-3} mbar chamber pressure. The bonded area in a single chip was approximately $9,503\text{ mm}^2$ and the bond strength between the two electrode was allocated at $33,95\text{ MPa}$ by tensile strength measurement method. The bonded wafer pair was slicing up for chips and than packaged in a socket (TO8 Schott). Following the packaging, the trench for the outlet of the fix electrode was being filled up. The relative pressure sensor was formed through a hermetical separation of the cavity from the outer atmosphere.

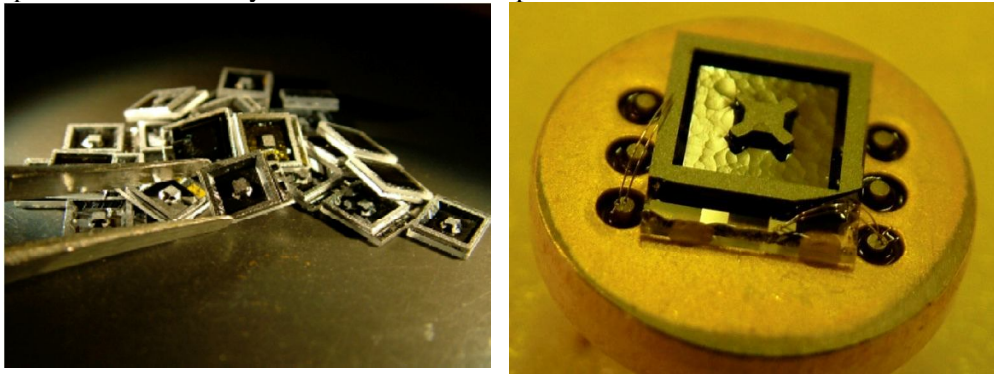


Figure 4. Assembled and packaged capacitive pressure sensors.

The fabricated and packaged capacitance pressure sensors (see Fig. 4.) were functionally tested in the working pressure range. The output capacity was measured under pressure range of $80\text{ to }1000\text{ mbar}$. As required the device had near linear response in the measured pressure range as presented in Fig. 5. The general properties of the capacitive pressure sensor are showed in Table 1.

Table I. Datasheet of the MEMS capacitive pressure sensor

Pressure Range [mbar]	Pressure Measurement	Sensing Structure	Thermal Sensitivity	Signal Output	Size [mm]
1-10; 10-50; 50-250; 250-1000;	Absolute Ref.: 1 atm	$10\text{ }\mu\text{m}$ thick Si membrane	No	Capacitive	$5 \times 6 \times 1$
Response Capacity [pF]	Sensitivity [fF/mbar]				
1-10	2-4				

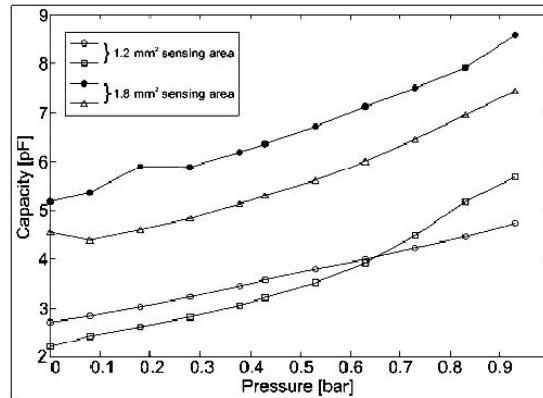


Figure 5. Test characteristics of the pressure sensor.

Application of nanosize hexagonal WO₃ sensing layer in MEMS based gas sensor

A. E. Pap, R. Csutak, A. Adam, and J. Pfeifer

Metal -oxide semiconductor gas sensors are of significant interest to detect toxic and hazardous gases. Nowadays the energy efficiency, small dimensions, low cost and high reliability may be the most significant requirements for electronic gas sensing devices, to be adequate in industrial and commercial applications. The use of small and cheap devices is preferable since a large number of sensors can be placed easily to different sites to monitor the concentration of different species without involving huge investments.

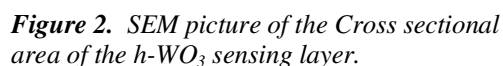
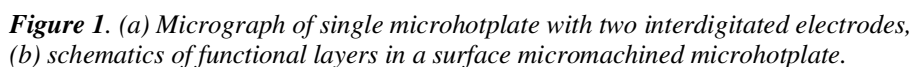
Heatable suspended membrane systems have been developed at MTA MEMS laboratory which temperatures reach few hundred degrees of Celsius by several mW of electric power. These devices with a suitable sensing layer may be adequate to achieve the expectations mentioned above.

Among of other semiconducting metal oxides, tungsten trioxide is the most promising material for gas sensing applications as an active layer.

Crystalline hexagonal-WO₃ (h-WO₃) powder was prepared by J. Pfeifer and co-workers at Ceramics and Nanocomposites Department of Research Institute for Technical Physics and Material Science. They investigated the response of the sensing material under exposure of organic vapors and NO_x gases. Results show that the sensitivity of the wet processed h-WO₃ to NO_x gases at temperature of as low as 150 °C is outstanding. In our development we used this type of h-WO₃, as active layer which had been provided by Dr. J. Pfeifer.

The base structure of the solid state sensors were manufactured by single side bulk micromachining silicon technology. A single microhotplate element and its layer structure are illustrated in Fig 1. The most obvious features are the suspended hotplate, four support beams, and the etch pit. The device shown also has two comb-

During the test measurements sensor were exposed to continuous gas stream of 100 ppm $\text{NH}_3\text{-N}_2$ or clear N_2 gas by turns, in 30 minutes. The resistance of the semiconducting film at different temperatures was obtained by measuring the potential drop between the pins of the interdigitated electrodes whilst 1 μA direct current was driven through the active layer. The resulted curves (Fig. 3.) plotted the variation of the resistivity of the sensing layer as a function of the time for different hotplate temperature.



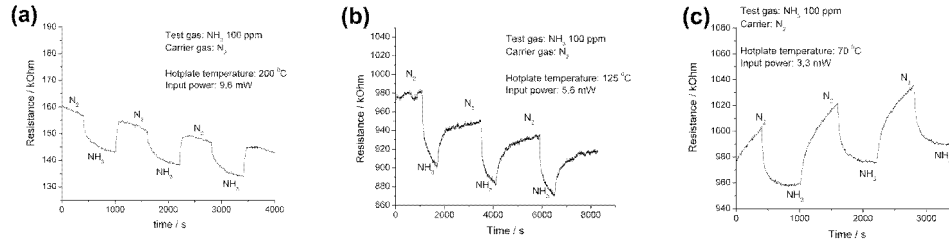


Figure 3. Time dependence of the resistance of the $h\text{-WO}_3$ active layer during exposure to 100 ppm NH_3 , in presence of nitrogen.

Shaping of micropatterned structures by anisotropic deformation under ion irradiation

Z. Zolnai, A. L. Tóth, and G. Battistig

Recent modern topics of micro- and nanotechnology relate to the fabrication of 2D or 3D arrays of hetero-structures built up from different elementary objects with regular shape and well-controlled size. There is an increasing demand for appropriate tools which can couple micro- and nanoscale dimensions as top-down or bottom-up

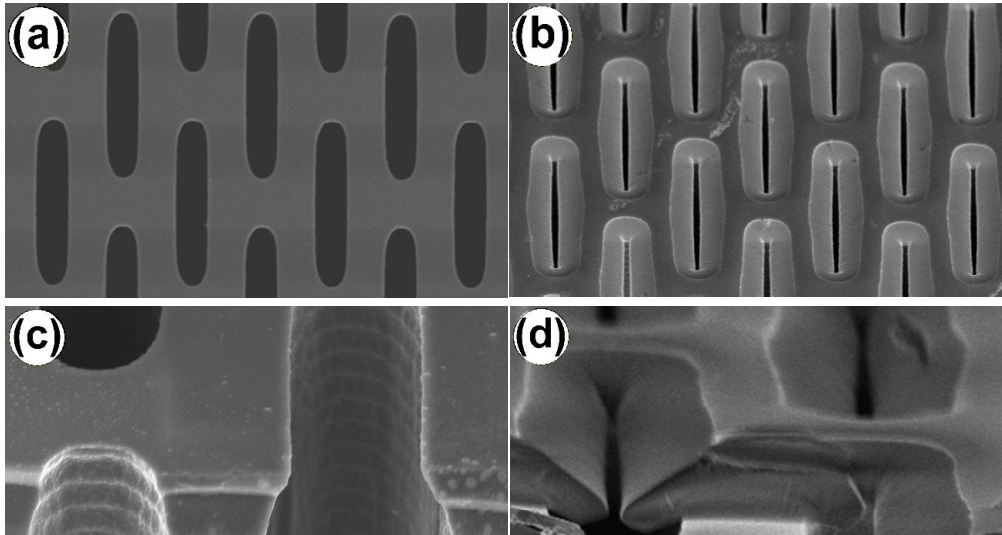


Figure 1. (a) SEM view of regular arrays of Si micropores formed by deep reactive ion etching (DRIE) through a silicon dioxide masking cap layer. The width and length of the pores is $3\ \mu\text{m}$ and $15\ \mu\text{m}$, respectively, with a spacing of $3\ \mu\text{m}$ in both directions (b) Similar view of the structure after irradiation carried out perpendicular to the sample surface with $2.8\ \text{MeV N}^+$ ions to a fluence of $1016/\text{cm}^2$. Here the slit between two facing edges is reduced to about $220\ \text{nm}$. (c) and (d) shows SEM side views recorded with higher magnification on the cross sectional edges of the samples shown in (a) and (b).

techniques, especially when particular applications call for specific solutions. As Fig. 1 shows, one example can be the formation of a horizontally continuous or nearly continuous planar-like cap layer on the top of micro-patterned surfaces of porous 3D Si structures. The aim should be to protect the pores as reservoirs from the ambient or to tailor the distance between two facing edges in order to control transport properties or optical coupling at the surface layer on sub-micron scale. The closing of surface slits can be realized by the so-called ion irradiation-induced plastic deformation (often called ion-hammering) process of silicon dioxide or amorphous silicon. In this case the irradiated layer contract parallel to the ion beam and expand perpendicular to the ion beam without significant volumetric change.

As the deformation rate can be finely tuned with the applied ion fluence, the ion hammering process should be considered as a successful one-step micro/nanofabrication tool. Note, high deformation rates can be achieved and no heat treatment of the sample is needed. The thickness of the transformed layer is determined by the penetration depth of the energetic ions, e.g. when a silicon dioxide layer is bombarded with N^+ projectiles of 2.8 MeV energy, a surface layer with thickness of about $3\ \mu\text{m}$ is exposed to the ion hammering process.

The parameters of shape transformation also depend on the type and energy of the ions as well as on the density and initial shape of the target, the temperature, and the direction of the ion beam with respect to the sample surface. Nevertheless, the phenomenological model of the anisotropic deformation process is well described and the mean features can be estimated as a function of the applied ion fluence [T. Van Dillen *et al.*, *Phys. Rev. B* **71**, 024103 (2005)].

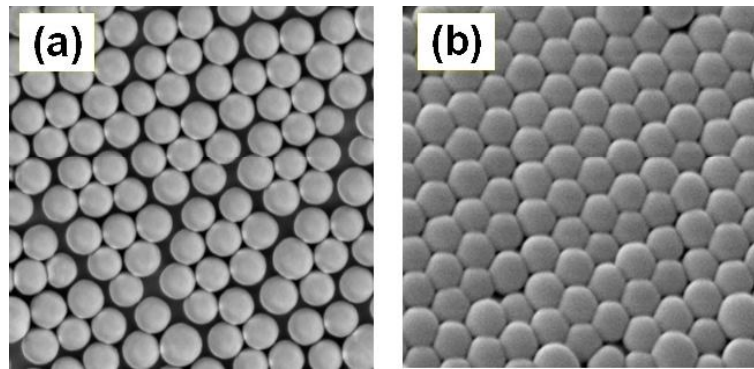


Figure 2. One monolayer of colloidal silica particles with diameter of $D = 450\ \text{nm}$ deposited on Si substrate with Langmuir-Blodgett technique (a) before and (b) after irradiation carried out perpendicular to the film plane with 500 keV Xe^{2+} ions to a fluence of $10^{16}/\text{cm}^2$. Due to irradiation induced plastic deformation, the particle shape changes from sphere to oblate ellipsoid with its minor axis parallel to the direction of the bombarding ion beam. For details see: Z. Zolnai *et al.*, *Phys. Rev. B* **83**, 233302 (2011) and Z. Zolnai *et. al*, *Nucl. Instrum. Methods in Phys. Res. B* **268**, 79-86 (2010)

Fig. 2 shows the result of the hammering effect when a monolayer of colloidal silica particles is irradiated with energetic Xe^{2+} ions. Here the particles undergo anisotropic deformation upon changing their shape from spherical to oblate ellipsoidal. Such

anisotropic particles can be applied as tunable photonic crystals [K. P. Velikov *et al*, *Appl. Phys. Lett.* **81** 838-840 (2002)] or as shadow nano-masks for the deposition of single dots on the underlying substrate through the holes of neighboring particles [D. L. J. Vossen *et al.*, *Nano Letters* **5** 1175-1179 (2005)]. Note, for 500 keV Xe²⁺ ions the penetration depth is about 350 nm into silica and almost the full fraction of the particle volume is exposed to the ion hammering process. Note, below a particle diameter of 200 nm the hammering effect is strongly reduced due to surface capillary forces [T. Van Dillen *et al.*, *Phys. Rev. B* **74**, 132103 (2006)].

Integration of buried channels in cerebral silicon microprobes

Z. Fekete, A. Pongrácz, and P. Fürjes

Microfluidic channels for local fluid injection or sampling integrated on silicon (Si) based neural multi-electrodes (see Fig. 1) are required for better understanding of different brain mechanisms during in-vivo experiments. Drug delivery systems buried underneath the Si surface is recommended to minimize the diameter of the probe and to keep the surgery minimally invasive. Simplified fabrication technology of completely buried passive microfluidic channels using dry etching methods is presented to meet the demands of today's complex microsystems. The applied process flow with selective edge-protection (patent pending) resulted in sealed microchannels while preserving the surface planarity above the buried structures as presented in Fig. 2.

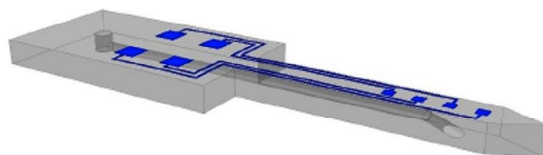


Figure 1. Artistic representation of the silicon microprobe with integrated buried microchannel for simultaneous drug delivery and electric measurements.

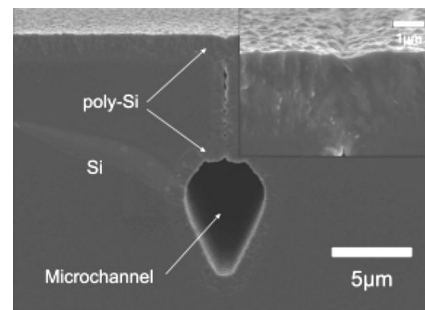


Figure 2. Cross-section of a buried microchannel realized by our group after the sealing by LPCVD poly-Si deposition is completed.

The formation mechanism of the predefined trench and the buried channel is characterized in details. The etching reaction forming the final geometric profile of the channel slows down generally with increasing aspect ratio of the predefining trench. The vertical component is influenced mainly by the depletion of the radicals. The horizontal etch rate is decreasing faster than the vertical, causing a more anisotropic cross section profile of the channel with increasing depth. We suppose that the horizontal etch rate is influenced not only by the depletion of the radicals, but

a highly decreasing horizontal ion flux is superposed, originating from the shadowing/collimating effect of the trench walls.

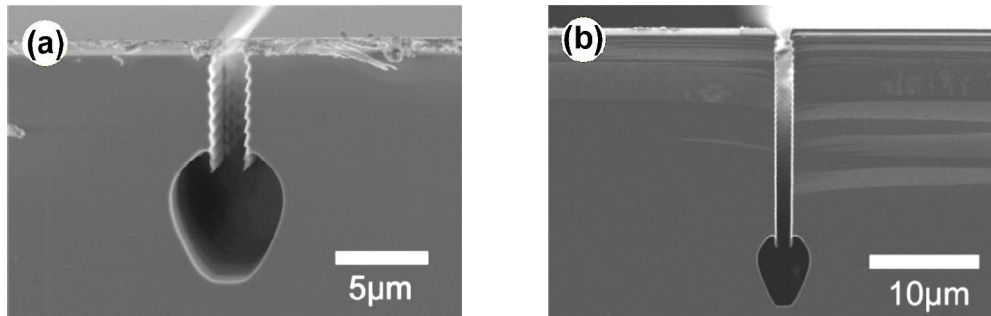


Figure 3. Profile of DRIE etched buried channels before trench-filling in case of aspect ratios 4:1 (a.) and 14:1 (b.).

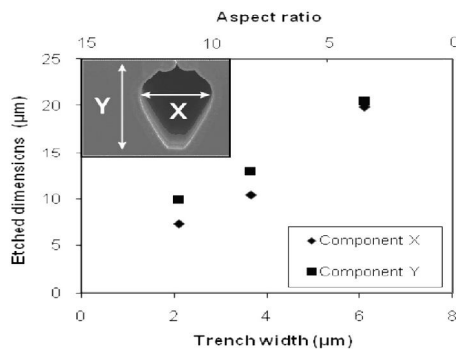


Figure 4. Change of etch components vs. final geometry of the trenches. Trench width is 2 μm.

The functional parameters of the proposed micro-needles as hydrodynamic resistance and mechanical stability were also characterized as the function of the geometrical parameters of the realized structures considering the technological limitations also. Experiments proved that aspect ratio of the predefined trench on the silicon wafer is a key parameter and should be carefully tuned in order to fabricate microchannels in microprobes in a reasonable way, fulfilling both mechanical and fluidic specifications.

Growth and properties of Al doped ALD ZnO

(OTKA NK73424)

Zs. Baji, Z. Lábadi, Z. E. Horváth, M. Fried, K. Vad, J. Tóth, and I. Bársony

ZnO has attracted great attention recently because of its versatility in a number of applications, such as sensors and photovoltaic devices. It can be doped with aluminium to increase its conductivity, and be used as transparent conductive oxide layer.

We developed an ALD process for the in situ Al doping of ZnO. The procedure consists of periodic alternate injection of Al-precursor pulses intermixed with the sequences of Zn-precursor pulses. The specific resistances of the ALD Al:ZnO layers were evaluated as a function of the introduced atomic fraction of Al (i.e. number of Al precursor pulses) and temperature. We examined in details the effects of Al doping on the layers in a wider doping and temperature range. We found that in the case of Si and glass substrates the ALD grown ZnO films are polycrystalline, and the deposition temperature determines the dominant crystalline orientation of the layers: At lower temperatures the (100) orientation is dominant, that is, the crystallites stand perpendicular to the surface. At higher temperatures the (002) peak becomes the dominant orientation, that is, the crystallites are parallel to the surface.

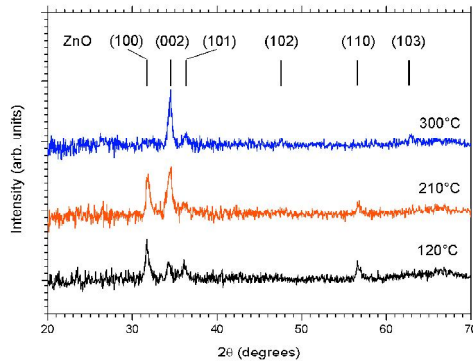


Figure 1. The orientation of the ZnO layers at different temperatures.

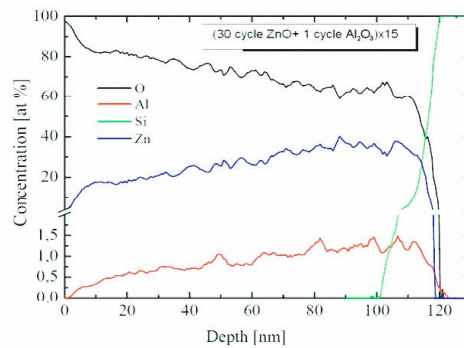


Figure 2. The SNMS depth profile of a doped layer.

Since the source of Al doping are the AlO_x sublayers, the Al content is not homogeneously distributed throughout the layer. Instead it rather forms a multilayered structure (as seen from the SNMS results).

XPS analysis of the layers show that the majority of the introduced Al is present in the form of AlO_x , and only a fraction of the Al (about 10%), is incorporated as electrically active dopant. However it is sufficient to reduce the resistivity of the intrinsic layers by two orders of magnitude. Sheet resistance of the best doped layers was as low as $9\text{E-}04 \text{ Ohmcm}$. Van der Pauw analysis of the samples showed that the carrier concentration monotonously increases with the increasing amount of electrically active aluminium, while the mobility monotonously decreases. This phenomenon results in an optimum of the resistivity as a function of introduced Al. As a function of the deposition temperature the carrier concentration develops a maximum, while the mobility decreases monotonously.

This optimum has also been established by the analysis of bandgap values from spectroscopic ellipsometry, and optical absorption results. The AlO_x doping linearly increases the band gap of the layers. As a function of the deposition temperature the band gap has a minimum. The most perfect crystal structure and largest grain size was found at 2 at% Al content at every growth temperature, while the accumulation of compressive strain developed a monotonous increase with the growth temperature.

The resistivity of the samples in lateral and normal directions develops similar qualitative tendencies. Despite this change in the orientation the conductivity shows no anisotropy, therefore we concluded that the conduction mechanism is not grain boundary related.

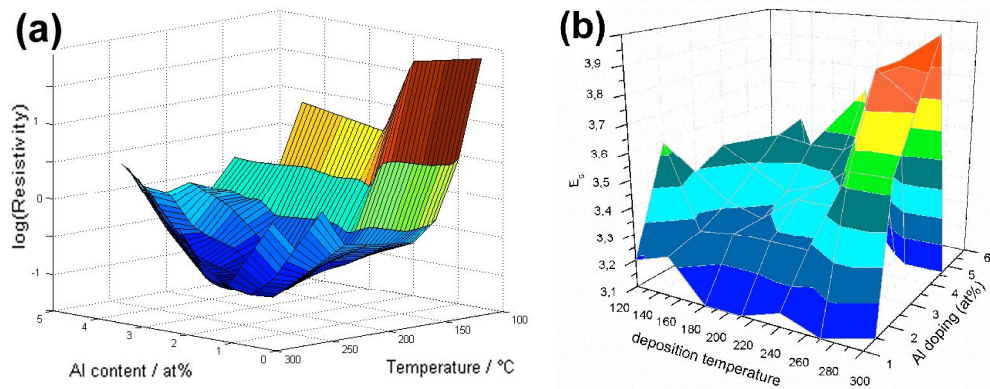


Figure 3. The resistivity (a) and the band gap (b) of the layers as a function of deposition temperature, and doping.

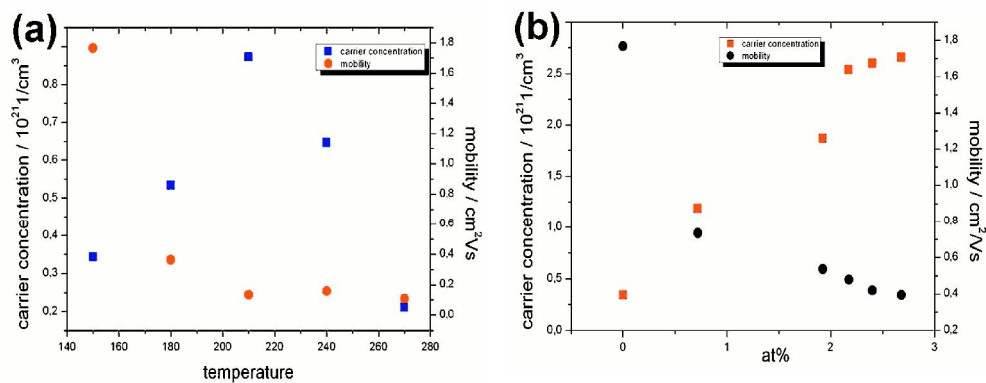


Figure 4. Carrier concentration and mobility of the layers as a function of temperature (a) and doping (b).

We have deposited ZnO layers on Si, GaN and sapphire substrates, and found completely different morphologies. Epitaxial growth is possible both on GaN and sapphire with a proper tuning of the deposition. The TEM micrograph below shows a cross section of the epitaxial ZnO layer on a sapphire substrate.

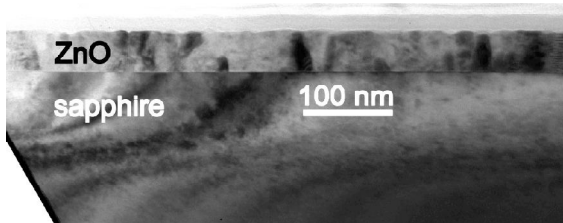


Figure 5. Epitaxial ZnO layer on sapphire (TEM micrograph).

Properties of CIGS films deposited by flash evaporation and post selenization

(OTKA NK73424)

Zs. Baji, Z. Lábadi, Gy. Molnár, A. L. Tóth, K. Vad, and I. Bársony

Chalcopyrite CuInGaSe materials are very promising candidates for photovoltaic applications due to their high absorption coefficients (10^5 cm^{-1}), long term electrical and thermal stability, and outstanding resistance against photo-degradation.

Post selenization of the precursors is a promising method for low cost large scale production of solar cells. Selenization is usually achieved by using Se vapour, or H_2Se . (The latter is highly toxic, therefore rises environmental and health concerns.)

The aim of our work is to present a new way of fabricating CIGS material by flash evaporation of Cu, In and Ga metal precursors from a single source followed by post-selenization. We studied the effect of CIG precursor morphology and selenization parameters on the CIGS material.

A new method was developed for evaporating the 3 metallic components from the same evaporating source, similar to using an alloy-like source, except that in our case the alloy forms only whilst heating the source. The best efficiency solar cells can be obtained with the following ratio of the components: In:Ga:Cu/0,,8:0,,2:1. For the post selenization of the layers CIG samples with Se pellets were sealed in 10^{-2} Torr vacuum, and annealed at 500°C in order to form the Cu(In,Ga)Se_2 phase.

The morphology and element distribution of the as deposited CIG precursor was studied by SEM microscopy using Electron Dispersive Spectra (EDS). Fig. 1. shows that the indium –which evaporated first- formed droplets on the surface, which were then covered with a uniform thin layer of gallium and copper..

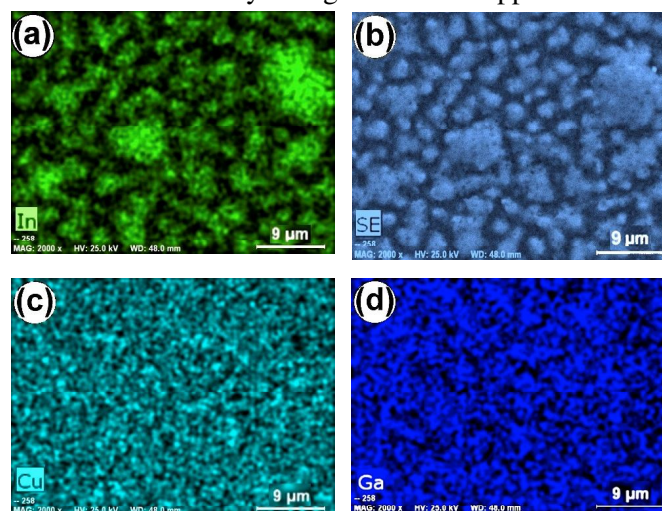


Figure 1. The morphology and element distribution of the as-deposited CIG layers. (Secondary electron micrographs: In (a), Se (b), Cu (c), and Ga (d) EDS maps.)

According to the literature, rough morphology of a co-evaporated CIG layer may deteriorate the resulting CIGS morphology, and thus the overall quality of the selenized CIGS film. Our layers, on the other hand, became homogenous after selenization (see Fig. 2), and their elemental composition is in agreement with the required CIGS composition, according to the literature.

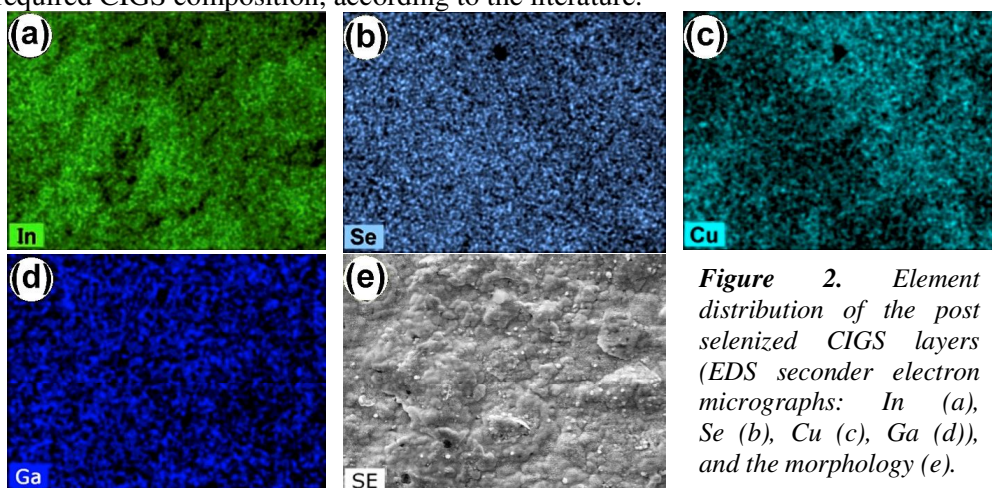
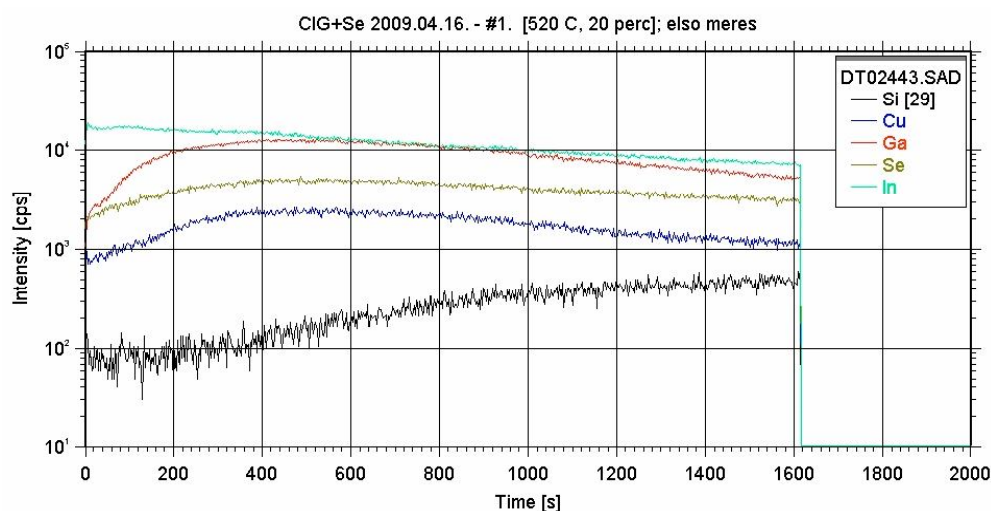


Figure 2. Element distribution of the post selenized CIGS layers (EDS secondary electron micrographs: In (a), Se (b), Cu (c), Ga (d)), and the morphology (e).

Another major drawback of the post-selenization method is that CIGS layers deposited by this technology tend to have excess Ga near the back contact of the layers, which decreases the overall device efficiency. Our samples, on the other hand, showed no sign of this effect, their composition is uniform throughout the film. On Fig. 3. It is shown the Secondary Neutral Mass Spectroscopy (SNMS) depth profile of our CIGS film.



File: DT02443.SAD
Date: 4/20/2009 12:13:42 PM

Figure 3. SNMS depth profile of the post-selenized CIGS layers.

LPE growth and characterization of InP/InGaAsP infrared emitting diodes

V. Rakovics, S. Püspöki, and I. Réti

Infrared LEDs have been rapidly achieving new applications in near infrared (NIR) spectroscopy. LED module based on a linear array of LED chips and a fixed monochromator provides a solid-state electrically scanned source for pre-dispersive spectrometers. NIR absorptions are most often associated with $-OH$, $-NH$, and $-CH$ functional groups. Also, absorptions due to electronic transitions of organometallic molecules in blood appear in the NIR. The emission spectra of different composition InP:InGaAs(P) LEDs can cover the 900–1700 nm wavelength range. In this work double heterostructure InP/InGaAs(P) LEDs were prepared to cover completely the 900–1700 nm wavelength range. Small area planar structures were fabricated for diode array application. The spacing of peak wavelengths was planned according to the spectral bandwidth of InP/InGaAsP LEDs. Unfortunately, the literature data for spectral bandwidths varied from 52 to 75 meV. At first, we used our previous data for planning the peak wavelengths of the LEDs chips. In the present work, we have deduced that the spectral bandwidth is strongly affected by the growth conditions. Narrow bandwidths can be obtained by choosing the appropriate growth temperature for each wavelength. InP/InGaAsP heterostructure diodes with uniform thick active layers, abrupt interfaces, and where the p–n junction was located inside the active region, showed narrow spectral bandwidths.

Double heterostructure InP/InGaAs(P) LED structures were grown by liquid phase epitaxy using (100) oriented InP substrate. The LEDs were grown in a computer controlled LPE apparatus equipped with multibin slider boat

Infrared transmission (Figs. 1-2) and photoluminescence measurements were used for the characterization of LPE-grown InGaAsP/InP LED wafers.

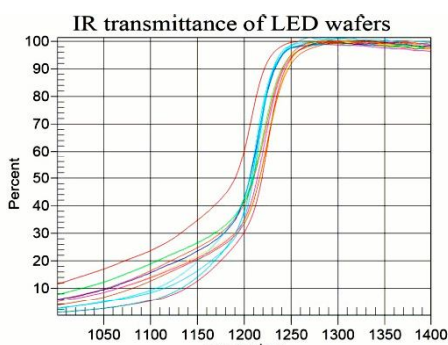


Figure 1. Infrared transmittance spectra of 1220-1230 nm LED wafers.

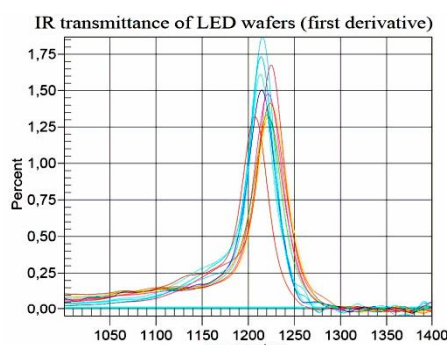


Figure 2. First derivative of the infrared transmittance spectra of 1220-1230 nm LED wafers.

The emission spectra of the mounted devices were measured at different driving currents (Fig. 3) and temperatures (Fig. 4). The current heating effect was taken into

account by extrapolation to zero current. The optical band gap was found to be strongly correlated with the extrapolated peak energy of the emission spectrum. Infrared transmittance measurements therefore offer a fast, reliable, and non-destructive way for the determination of the device emission wavelength using a wafer characterization method.

LED devices emitting below 1000nm were investigated carefully because their efficiency were lower than the efficiencies of long wavelength LEDs. The emission spectra of different LED's were compared with each other (Fig 5). The full width at half maximum (FWHM) for a 979 nm LED is considerably smaller than the same parameter for the 1008 nm device. Optical absorption of the substrate is responsible for the loss of efficiency. Optical transmittance spectrum of the InP wafer can be seen in Fig. 6.

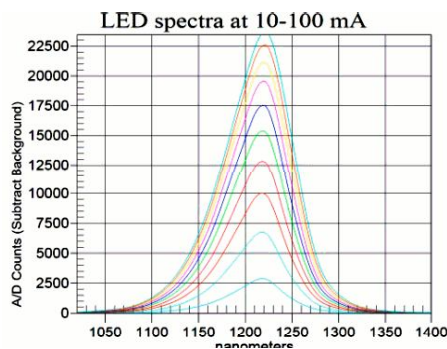


Figure 3. Emission spectra of 1220 nm LED at 10-100 mA driving.

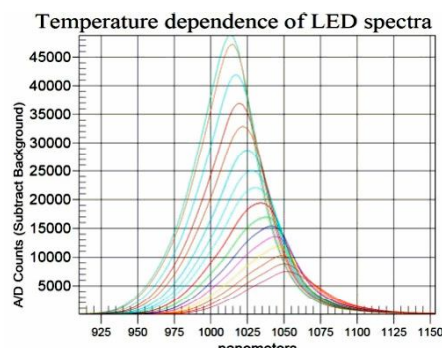


Figure 4. Emission spectra of 1020 nm LED at 23-180 °C.

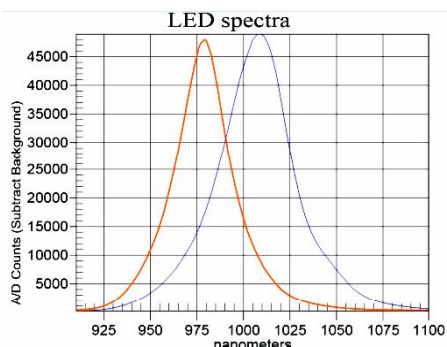


Figure 5. Emission spectra of short wavelength LED's.

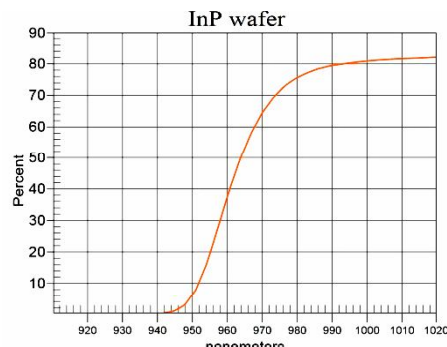


Figure 6. Optical transmittance spectrum of the InP wafer.

Activity in the joint MBE laboratory: investigations of the droplet-epitaxially grown nano-structures and equipment developments

Á. Nemcsics, I. Réti, P. Harmat, L. Tóth, M. Csutorás, G. Bátori, B. Plósz, L. Dobos, A. Ürmös, B. Pődör, S. Gruber, F. Pruzsina, P. Kucsera, G. Tényi, T. Sándor, J. Balázs, J. Makai, B. Kupás-Deák, and L. Nagy

Droplet-epitaxial nano-structures: In our project, nano-structures (such as quantum dot, quantum ring and nano hole) grown on AlGaAs (001) surface, were investigated (in-situ by RHEED and ex-situ by AFM, TEM and PL). In this year, inverted droplet-epitaxially grown quantum dot was investigated by TEM and PL methods (Fig. 1.). Here, the faceting and the growth kinetics were determined. The inverted quantum dot was prepared with the filling of the nano hole. We investigated the evolution kinetics of the nano holes and the quantum rings, too. The RHEED has also many open questions. Hysteretic phenomena of the RHEED intensity was modelled and explained for GaAs (001) and InAs (001) surfaces (Fig. 2.).

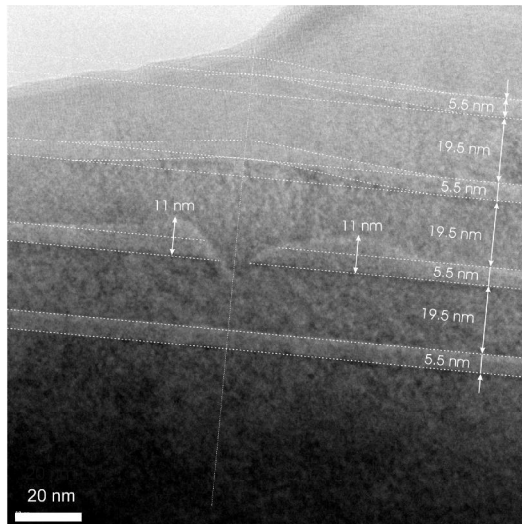


Figure 1. TEM picture of an inverted quantum dot.

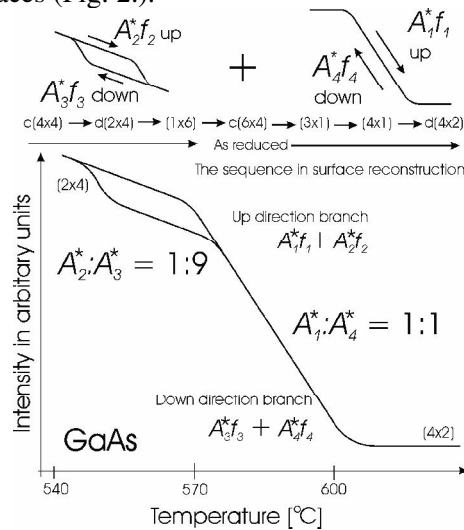


Figure 2. Hysteretic behaviour of the GaAs (001) surface

Developments on the MBE machine: In this year, we got and installed a QMS (QMG 220F3) for the residual gas analysis, and a gate valve (VAT 10844-E01) for the separation of the turbo molecular pump of the main chamber (Fig. 4). Furthermore, we developed a mechanical and electronic control (PLC) of the shutter movement (Knudsen cells). Computer visualization was developed for the MBE processes (Fig. 3.). The outgassing of the UHV chambers was improved with a boxing. Boxes were developed for the covering of the very complicated UHV chambers (Fig. 5). A movable CCD camera holder was developed for the RHEED evaluation. A computer program for the in-situ RHEED evaluation was developed (Fig. 6.).



Figure 3. Visualization of the control (above).

Figure 4. The main chamber with the QMS (left).

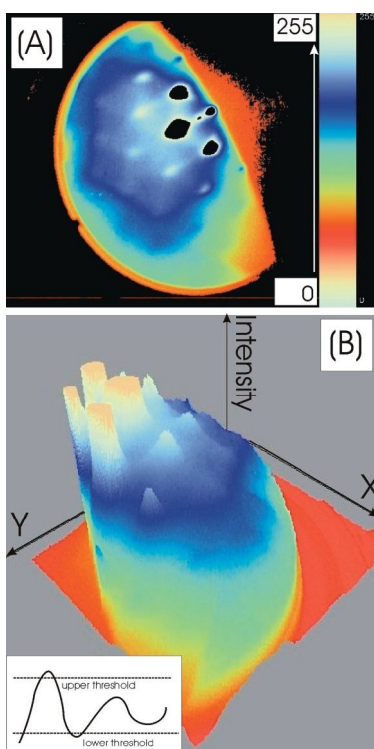
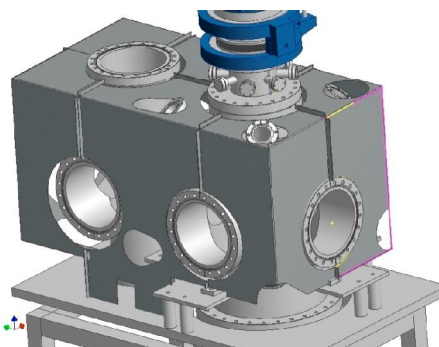


Figure 5. Chamber cover for the outheating (above).

Figure 6. The RHEED evaluation (left).



High sensitivity scanning probe capacitance sensing

L. Dózsa, G. Molnár, and Š. Lányi,

Introduction: DLTS using a special preamplifier measured with a scanned sharp tip and over a semiconductor surface was proved to be sensitive enough to detect point defects. C-V and I-V measurements of the scanning tip over a clean silicon surface were carried out under different conditions to better understand the effects of the different parameters on the local C-V and I-V measurements.

Experimental setup: The employed Deep-Level Transient Spectrometer contains a sensitive capacitance meter working at 1 MHz using a 0.1V measuring signal. A preamplifier with a gain 50 at 1 MHz increases the capacitance resolution to 1 aF (10^{-18} F) and its dc gain (1000) increases the dc current resolution to 1 pA. An 80 μm thick tungsten wire was sharpened in KOH solution to 50 nm radius and is fixed in a 110 μm internal diameter by friction. Coarse approach of the tip is made manually using a microscope. The fine positioning of the tip was tuned by observing and setting the tunnelling current measured at +2 V bias.

Results: C-V and I-V measurements carried out on Si wafers with 10^{16} cm^{-3} n-type dopant level are shown in Fig. 1. The scans are made starting at -5 V. The curves resemble a quasi-static C-V MOS with high density of interface states. Similar C-V curves were observed when dc current was below 10 pA at +2V bias. In this region the I-V characteristics are symmetric. These type measurements can be used for testing the surface potential and density of interface states, for example distinguishing different phases (insulator, metallic, semiconductor), but not for characterization of semiconductor electric transport properties or defects in the semiconductor below the tip. Fig. 2 shows typical C-V curves measured with smaller tip/surface distance. Such curves are typical when the forward current at +2 V is above 10 pA but below 500 pA. The C-V and I-V curves are Schottky barrier-like, with rectification character. The capacitance at positive bias tends to be in accumulation, the capacitance is limited by the air gap. This region is appropriate for the regular I-V and C-V characterization, since the current flowing through the semiconductor locally changes the charge distribution in the semiconductor near the tip. When the tip current exceeds about 500 pA the tip-silicon junctions degrades in a short time, the current becomes noisy, and I-V and C-V curves are not repeatable. This region is not useful for characterization. Measurements following prolonged biasing strongly changed the interface states at the surface of the silicon or the tip as it is shown in Fig. 3, after applying different bias' for 1 minute. The accumulation capacitance is strongly affected, surface charge changes.

Fig. 4 shows that the structure is sensitive to atmosphere. The interface states of the sample were strongly changed when the chamber is filled with air.

At negative bias inversion develops at the surface, which reduces the width of the depletion layer. This is demonstrated by the observed effect of light shown in Fig. 5. White light enhances the generation of electron-hole pairs thus developing inversion layer. In planar MOS capacitors in inversion the capacitance approaches at low

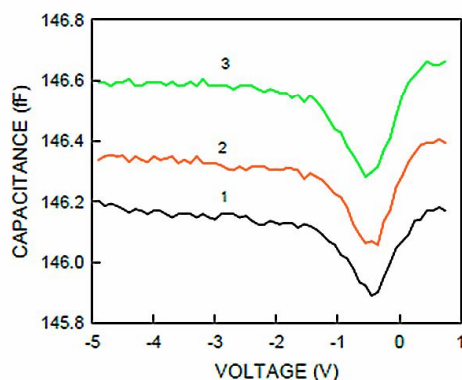


Figure 1. MOS-type C-V curves measured when tunneling current at +2V is below 10 pA. The tip/surface distance decreases from 1 to 3.

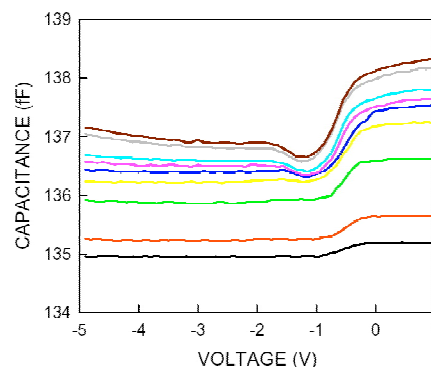


Figure 2. C-V curves with decreasing tip/surface distance when at +2V the tunneling current is below 500 pA, and rectifying I-V characteristics are measured.

frequencies a constant value, essentially equal to the accumulation capacitance. A high quality oxide would passivate most interface states. In a measurement on free surface the defect states at the semiconductor/insulator, their density may be very high. Some of them are related to the humidity, explaining the differences found in air and vacuum (Fig. 4). The disappearing of accumulation capacitance after biasing the sample by negative voltage can be explained by flat band shift, caused by charge trapped in surface states. This type of measurements offers a unique possibility to analyse the local density of surface states and defects in the semiconductor.

In most cases the capacitance modulation was rather small, indicating the magnitude of the stray capacitance. With the present probe, depending on actual protrusion of the tungsten wire from its holder, it was 136 to 146 fF. The changes indicate that capacitance measurement is not a secure way to position of the probe. Monitoring the tunnelling current was found to be more reliable, however, insulating island or particles on the surface may also lead to damage of the tip.

Conclusions: The capacitance and current measurement sensitivity of DLTS instrument has been increased using a preamplifier. Fine positioning the tip with a piezo scanner local C-V and dc I-V measurements could be carried out using a sharp tungsten tip at room temperature. The sensitivity is high enough to measured effects of a single elementary charge trapped on the surface, so the measured 'large signal' may be related to a few atomic interactions. Depending on the tip/surface separation 3 type of measurements may be worth to developed on the base of the setup, depending on possible budget and other strategic goals:

- At low tunnelling current (in our setup below 10 pA) the C-V shows a MOS characteristics. The current in forward and reverse bias is nearly symmetric, i.e. the current flowing through the tip does not significantly change the density of states in the semiconductor. This type of measurement can distinguish different surface phases (insulators, semiconductors with possibility to measure their gap, metals).

- At tunnelling currents exceeding 10 pA but below 500 nA the characteristics are similar to a Schottky junctions. The measured capacitance depends on the history of applied voltage, induced by atoms trapped on the surface. Scanning tip electrical characterisation of the semiconductor is viable in this case, however, it is very sensitive to the surface cleanliness. Presently the change of temperature is not possible since it makes the control of the tip-surface distance very difficult, due to thermal expansion and to mechanical stress.
- The I-V and C-V characteristics are not stable when the current at + 2V bias is above 500 pA, the tip-semiconductor interface it is visible degraded. This type of measurements may be interesting for understanding the interaction of the tip-surface, since the industrial standard scanning tip measurements often use this bias region without control in order to reach high sensitivity.

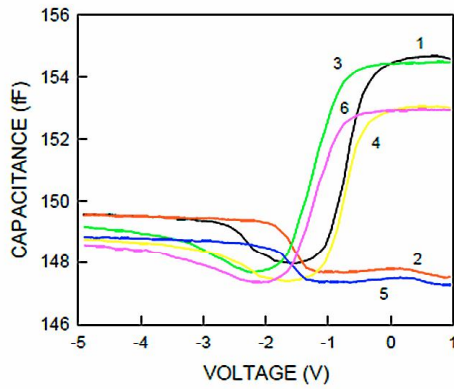


Figure 3. C-V curves measured after holding the tip bias for 1 min at: (1) 0 V, (2) -2 V, (3) +1 V, (4) 0 V, (5) -2 V, (6) +1 V.

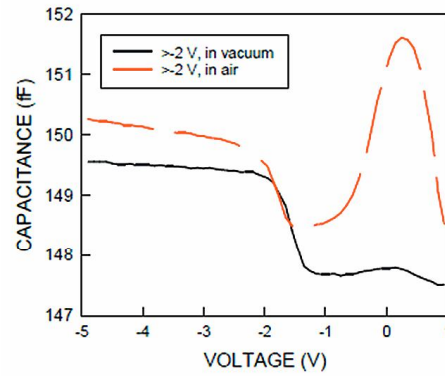


Figure 4. C-V measurement after -2 V bias of tip for 1 minute in vacuum (black) and in air (red/dashed).

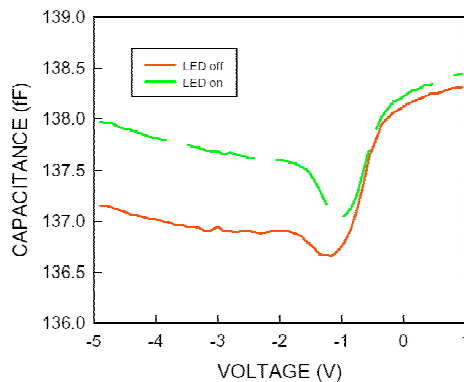


Figure 5. The effect of illumination by white LED. The light increases the inversion (generation of minority carriers) near the tip.

Integrated solid-state nanopores for biochemical sensing applications

(ENIAC JU CAJAL4EU, OTKA NF69262)

R. E. Gyurcsányi, Z. Fekete, A. L. Tóth, L. Illés, and P. Fürjes

The micro and nanotechnology based biosensing principles enable the development and realisation robust, user-friendly and cost-effective in-vitro diagnostic platforms. Furthermore, label-free and multi-analyte detection is envisioned to allow more accuracy and mass parallelism in clinical diagnostic. The final goal of this work is to develop nanopore based multi-parametric biosensing platform, applicable for label-free detection of blood marker proteins of cardiovascular symptoms, taking advantage of the built-in transport-modulation-based amplification mechanism.

Here we are presenting a line of nanopore based sensor development, including methodologies for fabrication and functional characterization of single channel solid state nanopores with diameters ranging from 5 to 100nm, their chemical modification and application for bio(chemical) sensing. Solid state single nanopores were fabricated by the combination of silicon micromachining and subsequent Focused Ion Beam nanofabrication processes considering the chemical, electrical and mechanical requirements.

The mechanical layer structures were realized by wet alkaline or double step Deep Reaction Ion Etching process respectively demonstrated in Figs. 1(a) and 1(b). Considering the nanopore based electrochemical metrology described high electrical and chemical resistance of the mechanical layers are crucial requirements. To ensure enhanced both chemical and electrical resistance and low residual stress a SiO_2 / SiN_x stacked supporting membrane with adequate layer thickness ratio was realized.

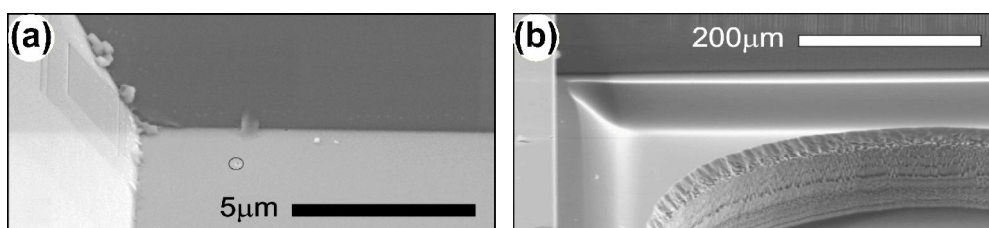


Figure 1. Layer structures realized by wet alkaline etching (a) and double-step DRIE process (b).

According to the biochemical application the structure of the realized nanopore transducers is absolutely critical regarding the possible receptor immobilization techniques. To discover and verify the adequate deposition chemistries different material structures were designed and fabricated. The supporting membrane material composition was already chosen to ensure low stress mechanical structures, but the functional layer of the nanopore was altered as Fig. 2 represents.

- Gold nanopores for thiol chemistry: in this case the nanopores were drilled in the vacuum evaporated Gold layer, which enable to apply thiol chemistry for the receptor immobilisation. (a)
- Silicon-Nitride nanopores for fluoro-alkil passivation tests: surfaces were passivated by fluoro-alkil chemistry (CEA-LETI) and the nanopores were drilled subsequently in the Silicon-Nitride (b)
- Poly-Silicon nanopores for electrografting tests: the nanopores were drilled in Poly-Silicon layer and the immobilisation were proceed by electrografting (c)
- Silicon-Dioxide nanopores for silanisation chemistry: the nanopores were drilled in Silicon-Nitride layer passivated by Gold, and shrunk by EBAD (electron-beam assisted deposition) grown TEOS Silicon-Dioxide. (d)

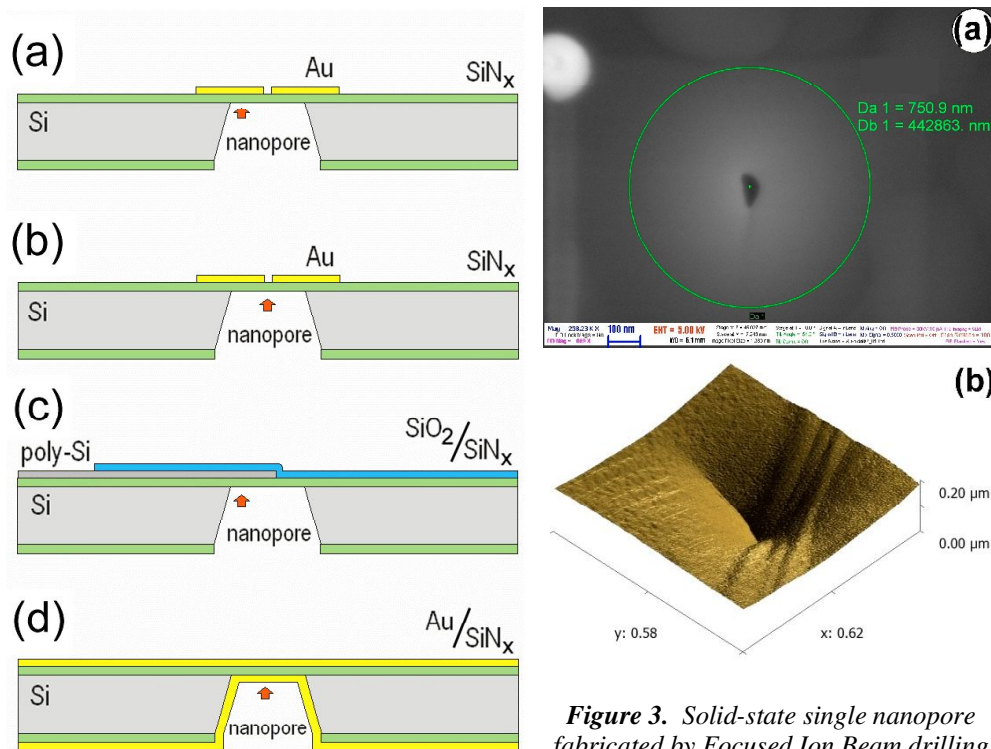


Figure 2. Designed and fabricated nanopore structures for different immobilisation chemistries.

Figure 3. Solid-state single nanopore fabricated by Focused Ion Beam drilling and subsequent selective electron-beam induced oxide deposition from TEOS gas: SEM image (a), AFM profile (b).

The wafer level fabrication of the sensor unit is also described, considering the integrability of the silicon based solid state device consisting 3D fluidic connections, microfluidic system and nanoscale sensing transducers too. The schematic representation of the 3D microfluidic system and its assembling on the microfluidic flow-cell is shown in Fig. 4. The vertical fluidic connects ensure the addressing of the two sides of the nanopore membrane electrically through electrolyte solution and the injection of the sample analyte too.

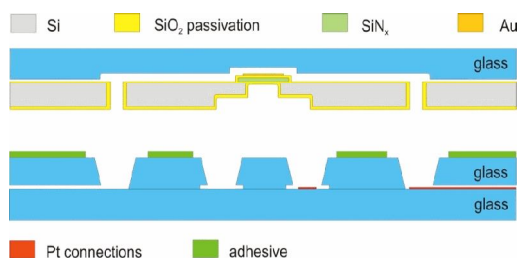


Figure 4. Schematic cross-sectional and back side view of the proposed nanopore membrane structure integrable into the transport microfluidic system.

The realized silicon structure was anodically bonded to the glass microfluidics in wafer level applying adequate working parameters (temperature, chamber pressure) limited by the integrated materials (gold) and thin layer structure. The solid state nanopores were fabricated by Focused Ion Beam milling subsequently in chip level and the final stacked structure was bonded onto fluidic connection platform designed and realized by the Micronit Microfluidics BV. This flow-cell is equipped with platinum electrodes, so the glass flow-cell and the silicon/glass sensor system are forming the sample loading and read-out system cooperatively, containing the fluidic and electrical addressing lines. The achieved structures are presented in Fig. 5.

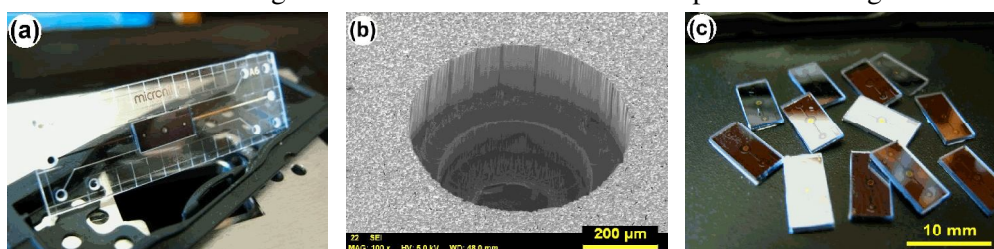


Figure 5. The back side fluidic connections (a) of the bonded silicon-glass chips (b), and the glass microfluidic flow-cell (c) with the mounted nanopore platform.

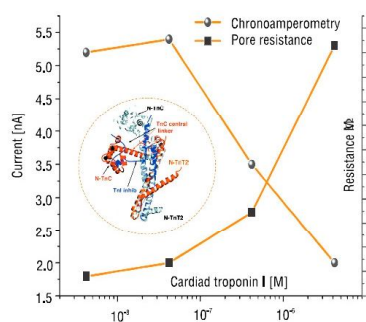


Figure 6. Sensor response for Cardiac Troponin-I applying artificial aptamer receptors.

To apply nanopores as selective detectors their inner surfaces must be chemically modified by specific receptors. Aspects of thiol (dithiolan disulfide) chemistries for building up self-assembled molecular architectures with molecular recognition capabilities are discussed in case of the gold nanopores. The applicability of the solid state nanopores for biochemical sensing was modeled and verified by coupling Gold-Streptavidin nanoparticle conjugates on the biotinated nanopores and by detection of the cardiac Troponin-I as the biomarker of the Cardio-Vascular Diseases applying artificial aptamer receptors (Fig. 6).

Separation of biological samples in microscale

(ENIAC JU CAJAL4EU, OTKA NF69262)

Z. Fekete, G. Huszka, F. Tolner, and P. Fürjes

Significant number of the clinical test is aimed to quantitatively or qualitatively analyse the presence of proteins, ions, crystalloids or diluted gases in human blood. In this case, the presence of blood cells in the sample could be a serious drawback, so the first stage of the tests must be the separation of plasma or serum from the whole blood in order to provide adequate sensitivity of measurements.

When aiming a complete microfluidic analysis system for human blood tests the blood plasma separation should be preferably also integrated in the device, so in this work the performance of microfluidic test structures utilizing the Zweifach-Fung effect in terms of two performance metrics: separation (SE) and purity efficiency (PE). These terms are defined as follows.

$$SE = \frac{V_{plasma}}{V_{plasma} + V_{cell}}$$

where V_{plasma} is the volume of sample liquid flowing through the plasma branch of a bifurcation, and V_{cell} represents the collected sample from the main channel.

$$PE = 1 - \frac{C_{plasma}}{C_{in}}$$

where C_{in} and C_{plasma} are the concentration of particle in the inlet and plasma branch respectively.

A series of silicon-glass based microfluidic chip was designed and fabricated by conventional MEMS technology. The influence of geometric parameters of several bifurcation arrangements was quantitatively analyzed under different flow conditions. Finite element modelling of the fluid flow in the vicinity of the bifurcations is also implemented to help the understanding of the experimental results. Our work contributes to optimal geometric design of separation components of microfluidic based diagnostic chips.

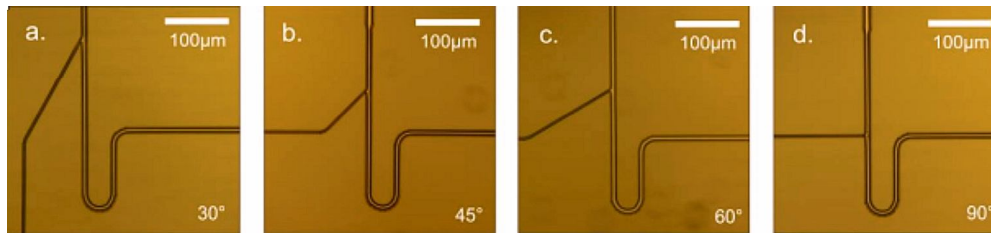


Figure 1. Filtering test structures with different bifurcation angles: 30° (a), 45° (b), 60° (c), and 90° (d), fabricated in silicon. The input stream is to be considered from the top in each microscopic view of the bifurcations.

The microfluidic channel system and the backside fluidic vias (inlets & outlets) of the separation chip is etched by the Bosch-process of deep reactive ion etching (DRIE). The silicon wafer is anodically bonded to a borosilicate glass substrate, which serves

as a sealing layer on top of the microfluidics. A representative SEM micrograph of a DRIE etched bifurcation and vertical via are illustrated in Fig. 2.

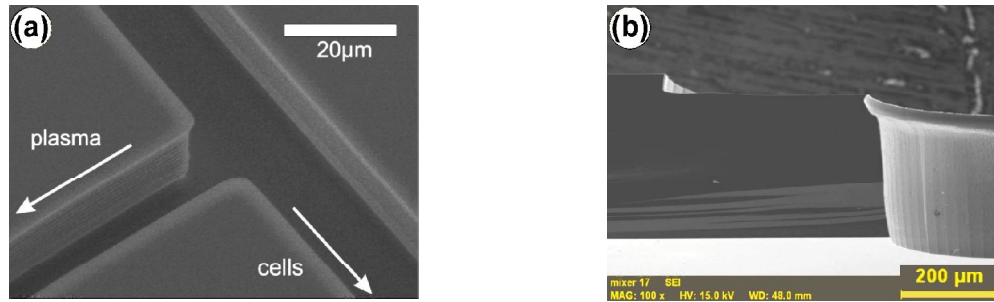


Figure 2. SEM view of a bifurcation (a) and the cross-section of the vertical via (b) in silicon fabricated by deep reactive ion etching.

We found that increasing flow rate ratio between bifurcation branches increase purity, but degrade efficiency of the system, therefore a compromise should be made, when both purity and high throughput are required in clinical applications. The effect is more remarkable, if plasma channels are getting thinner. The angle of bifurcation should be also considered, since at higher inclination angle the purity deteriorates. The proposed results of the characterization support the future design of cascade type separation systems.

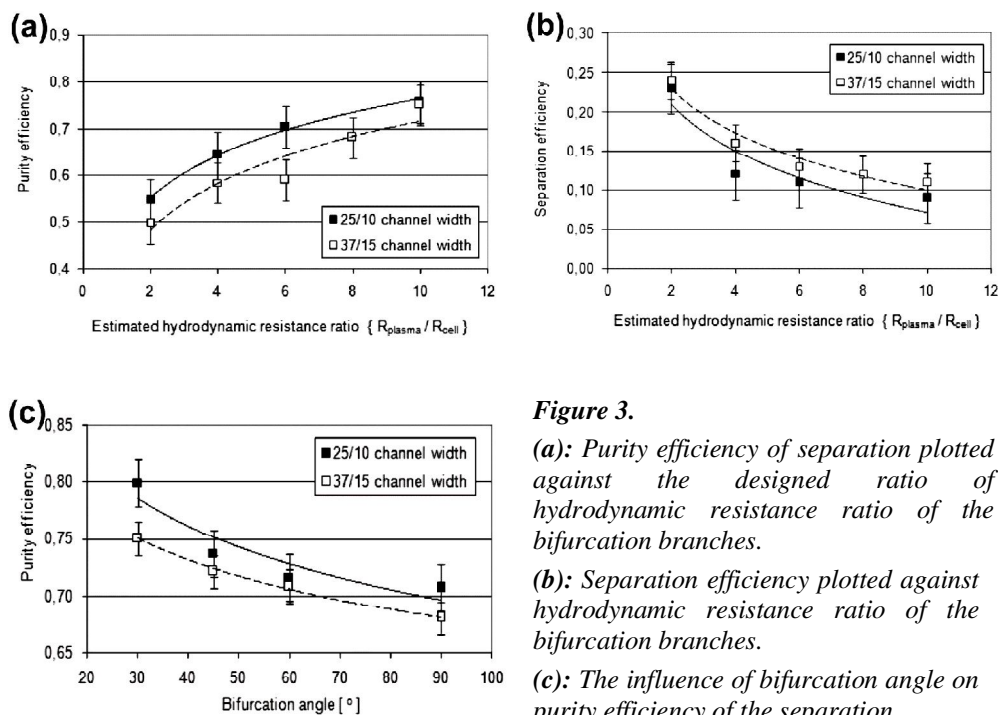


Figure 3.

(a): Purity efficiency of separation plotted against the designed ratio of hydrodynamic resistance ratio of the bifurcation branches.

(b): Separation efficiency plotted against hydrodynamic resistance ratio of the bifurcation branches.

(c): The influence of bifurcation angle on purity efficiency of the separation.

Design and process development of polymer based microfluidics for photonic biosensors

(EU FP7 P3SENS)

Z. Fekete, E. Holczer, and P. Fürjes

In this work, we report advances in the fabrication technology and testing of polymer microfluidics as a part of a polymer biosensor photonic device developed in the European Union project P3SENS (FP7-ICT4-248304). The main target of the development is to design and realize robust microfluidic systems which are applicable for cost-effective sample transport and still can contain some simple sample preparation functions, such as washing, mixing or dilution.

The polymer based microfluidic structure was realised by fast prototyping applying SU-8 epoxy based negative photoresist as moulding replica for polydimethylsiloxane (PDMS) moulding. The PDMS is a silicon based organic polymer: $(\text{H}_3\text{C})_3[\text{Si}(\text{CH}_3)_2\text{O}]_n\text{Si}(\text{CH}_3)_3$ which is absolutely feasible to form microfluidic structures in bioanalytical applications due to its reliable geometric transfer, flexibility, transparency, biocompatibility and price, moreover it is beneficial for both the large scale production and fast prototyping. Disadvantages are the hydrophobic character (adsorption of hydrophobic ligands) and the possible long term degradation. An improved 3D multilayer formation process was developed in order to achieve reliable SU-8 structuring for the formation of high aspect ratio sidewalls and advanced functional elements of the microfluidic system. Moulding forms developed by multilayered SU-8 photoresist for chaotic mixer structures are presented in Fig. 1.

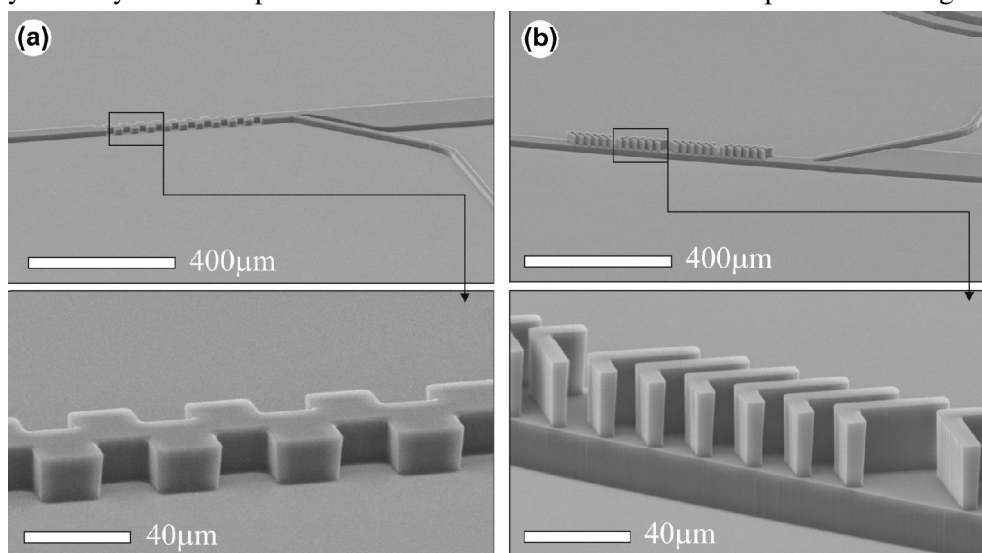


Figure 1. SU-8 moulding replica for the Staggered blocks (a.) and the Herring-Bone type (a) mixer structure fabricated by 3D multilayer technology.

Due to the low cost requirements of point-of-care applications, the photonic chip is fabricated from nano-composite polymeric materials, using highly scalable nano-imprint-lithography (NIL). The key issues investigated during the research from the point of the integrability and final applicability of the developed structures are an appropriate polymer material selection, which has a natural impact on the leakage-free bonding between the optical (sensing) and the fluidic (sample transport) part of the device. To obtain a stable and high adhesion between the fluidic and the optical units, several different materials (polyimide, poly(methyl-metacrylate), SU-8) and bonding strategies were qualified. Adequate adhesion were achieved by subsequent silanisation (applying organofunctional alkoxysilanes as (3-aminopropyl)-triethoxysilane – APTES) processes and oxygen plasma treatments applied for the polymer surfaces as illustrated in Fig. 2.

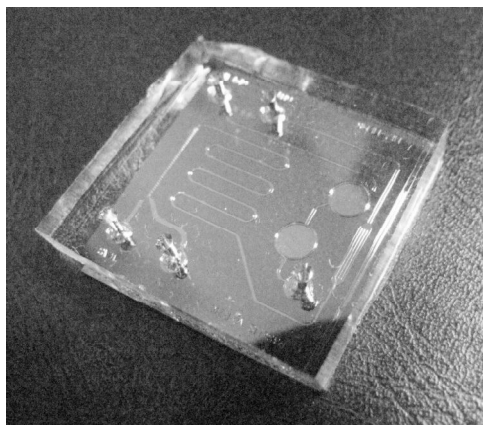


Figure 2. PDMS microfluidics bonded reliably onto the polymer surface of the photonic chip.

Surface modification in PDMS based microfluidic devices

(EU FP7 P3SENS)

E. Holczer, Z. Fekete, and P. Fürjes

Notable drawback of the application of PDMS in biosensors is the hydrophobic surface characteristics, significantly affecting the maximal flow rate in the channel system. Moreover, the non-specific binding of proteins or ligands on the channel surfaces is also a critical issue due to the possible depletion of the target molecules during the transport to the active sensing area of the device. Our work is also intended to define a modified material composition, which is appropriate to significantly improve both the wettability and the non-specific binding characteristics of PDMS. TX-100 surfactant was added to the raw PDMS before polymerization and the influence of the tenside was studied considering the polymerization reaction, the surface characteristics and the device functionality also.

A significant change in the contact angle was observed, which is attributable to the embedded TX-100 molecules. The decreasing in contact angles refers to the improvement of the wettability of PDMS surface, facilitating the design of microfluidics featured by enhanced capillarity. The change of the characteristic capillary pressure in these systems indicates a beneficial use in passive microfluidic pumps as well. Figure 1 represents the change of the PDMS surface from hydrophobic to hydrophilic (from positive to negative capillary pressure) in the case of different characteristic channel widths. The height of the microchannel was 20 μm , defined by the thickness of SU-8 2015 layer as molding replica.

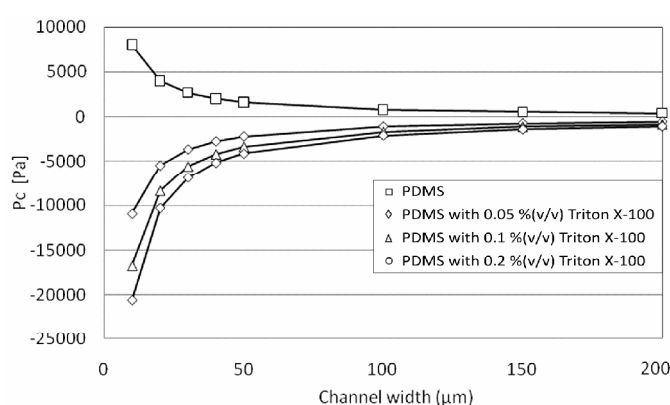


Figure 1. Representative capillary pressures in the modified PDMS micro-channels calculated from the measured contact angles.

The non-specific adsorption of proteins on the PDMS surface is crucial regarding the applicability of the microfluidic structure in bioanalytical systems. Accordingly, the binding of proteins to the channel sidewalls was characterized in case of different material compositions. To qualify PDMS from this aspect, surface adsorption of fluorescein-isothiocyanate (FITC) labeled HSA was recorded by measuring the time dependent change of fluorescent intensity detected in the microchannel by using a fluorescent microscope. Various compositions of PDMS and alternative surface blocking method were also tested. In Figure 2, the irreversible protein adsorption on different PDMS surfaces was characterized by recording the relative fluorescent intensity of the applied HSA. The recorded relative values were determined as intensity increments compared to the natural intensity of the HSA solution. Fluorescent intensity of 100% was detected, when PDMS surface was blocked by bovine serum albumin (BSA). The resident intensity after washing proves that irreversible HSA adsorption on the PDMS surface can be decreased by embedding TX-100 in the material.

We can conclude that non-specific protein adsorption can be decreased by almost 100% by this surface modification method parallel with the improvement of the capillary characteristics of the microfluidic system, although the application of additional surface blocking protocols is advantageous in sensitive bioanalytical measurements alike.

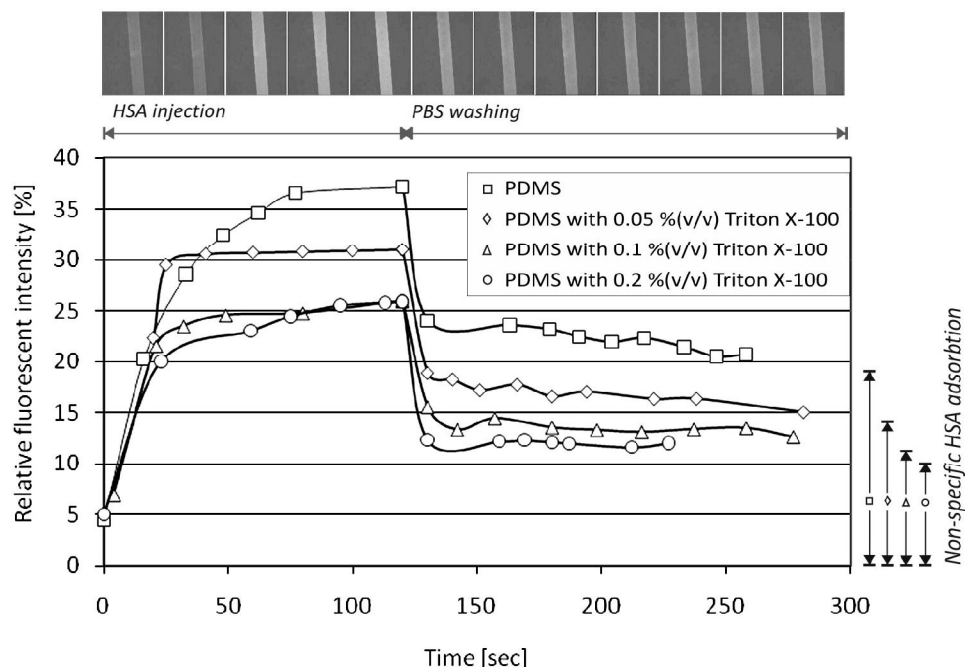


Figure 2. Adsorption of the fluorescent labelled HSA protein on different PDMS surfaces characterised by time dependent fluorescent intensity.

Chaotic mixing in polymer based microfluidics for bioanalytical system

(EU FP7 P3SENS)

Z. Fekete, E. Holczer, E. Tóth, K. Iván, and P. Fűrjes

Integrated microfluidic elements are essential components of all lab-on-a-chip devices. One of the important functions of the microfluidic system integrable into bioanalytical devices is the dilution and complete mixing of the analyte with an adequate buffer solution to ensure homogeneous concentration distribution of the species reaching the sensing area. The chaotic advection can be considered an ideal mixing method in the case of microfluidics where flows are stable and laminar.

Advection is the transport phenomenon generated by the fluid flow, where simple flows can cause a nonlinear or even chaotic distribution of molecules. The term chaotic advection refers to a transport phenomenon where advection, i.e. species transport is generated by the fluid flow in such a way that simple laminar flow velocity distribution leads to a chaotic behaviour of particle distribution without the need for turbulence.

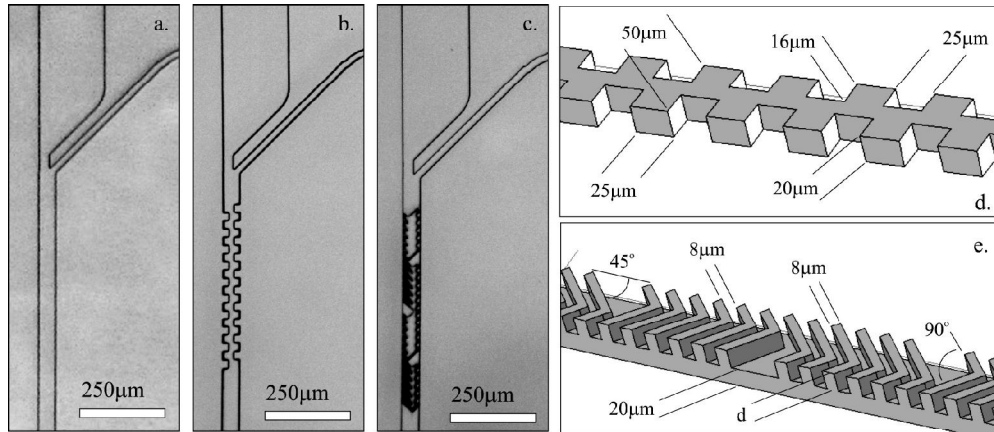


Figure 1. Realized mixer structures: T-mixer (a), T-mixer staggered blocks (b), Herring-Bone type (c) chaotic mixers. Applied geometric parameters for the modeling/design (d-e).

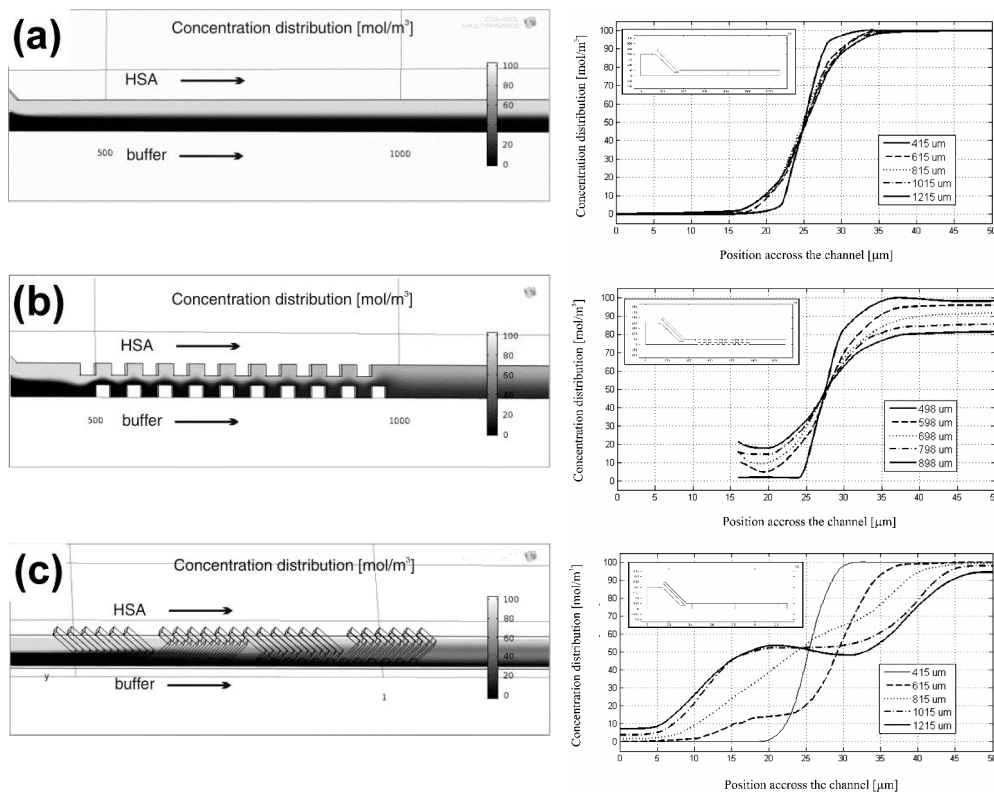


Figure 2. Concentration distributions of the analyte in the centerline of different surface slides (distances from the inlet indicated) of the mixer structures. (a): T-mixer, (b): T-mixer staggered blocks, (c): Herring-bone mixer. (On the left a qualitative view of simulated mixing is presented, while on the right the quantitative results are shown.)

The behavior of different chaotic mixer structures was analyzed by numerical modeling and experimentally to determine their practical efficiency. T-mixer staggered blocks (Fig. 1.b.) and Herring-Bone type (Fig. 1.c.) chaotic mixer structures realized by polymer fabrication technology were characterized by comparing them to a simple T-mixer as reference (Fig. 1.a.).

The fluidic behavior of these three different mixer structures was analyzed by Finite Element Modeling using COMSOL Multiphysics solving the Navier-Stokes and the diffusion equations. Initial boundary conditions were set to 0,1mM/mL concentration of human serum albumin solution and 2 $\mu\text{L}/\text{min}$ flow rate in each model. The calculated concentration distributions are presented in Fig. 2.

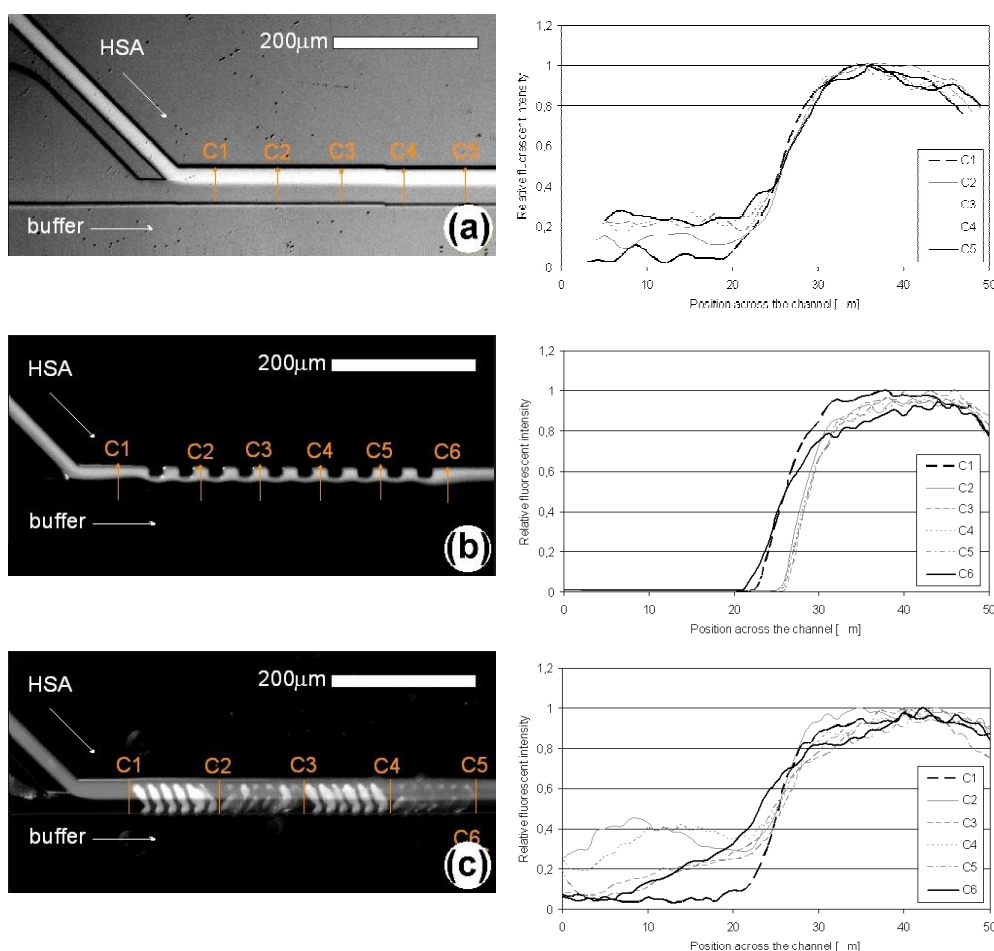


Figure 3. Concentration distributions of the analyte characterised by the fluorescent intensity in the centreline of different surface slides (distances from the inlet indicated) of the mixer structures. (a): T-mixer, (b): T-mixer staggered blocks, (c): Herring-Bone type mixer.

To create microfluidic structures in polydimethylsiloxane (PDMS), SU-8 epoxy based negative photoresist was used as a replica mould developed by a special multilayer technology (presented before) characterized by a channel width of $50\mu\text{m}$ and a depth of $20\mu\text{m}$. The fluidic channels with the reservoirs and the Herring-Bone mixer structure were formed by different SU-8 layers. The simulation results were verified by diluting fluorescent labeled human serum albumin (HSA) in phosphate buffered salt solution as presented in Figure 3. The channel surfaces were blocked by bovine serum albumin against the non-specific binding of the test proteins.

In the applied intermediate Reynolds number regime the characterized Herring-Bone type mixer shows the highest mixing efficiency in contrast with the staggered blocks mixer and the T-mixer applied as references. According to the results, the most promising mixer structures are the Herring-Bone type structures, although their mixing efficiencies are significantly influenced by the number of the V-groove blocks, due to the asymmetry of the proposed structure.

Design and characterisation of digital microfluidic chips

T. Pardy, Z. Fekete, and P. Fürjes

Compared to analogous microfluidics, digital microfluidics can operate with smaller – droplet-based - sample volume, while the functionality is programmable, since each elementary cell of the device is independently addressable. This flexibility offers large integrity in a bioanalytical chip involving sample preparation, transport and evaluation.

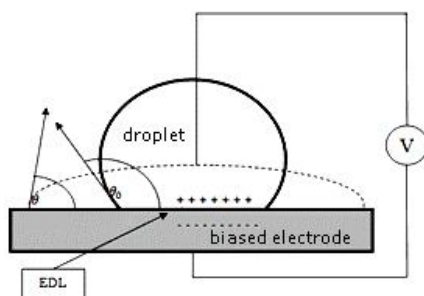


Figure 1. Principle of electrowetting. Changing the electric field on the boundary surface modifies the energy equilibrium, and the droplet turns from hydrophobic to hydrophilic state.

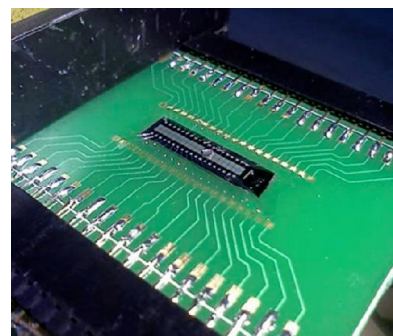


Figure 2. Experimental setup containing Si-based EWOD chip with linear layout mounted on a Printed Circuit Board providing the excitation to the cells.

Our group focuses on the optimization of electrode design using several test devices fabricated by standard MEMS technology. In cooperation with the Pázmány Péter Catholic University, motion frequency at several excitations is being analyzed both in linear and some complicated EWOD (Electro-wetting-on-dielectrics) chip layout, providing the separation and the mixing of functions, as necessary.